Local Lubrication Model for Spherical Particles within an Incompressible Navier-Stokes Flow

Baptiste Lambert, Lisl Weynans, Michel Bergmann

Local Lubrication Model for Spherical Particles within an Incompressible Navier-Stokes Flow

Baptiste Lambert, Lisl Weynans, Michel Bergmann

RESEARCH REPORT
N° 9093
September 2017
Project-Teams Memphis

ISSN 0249-6399 ISRN INRIA/RR--9093--FR+ENG

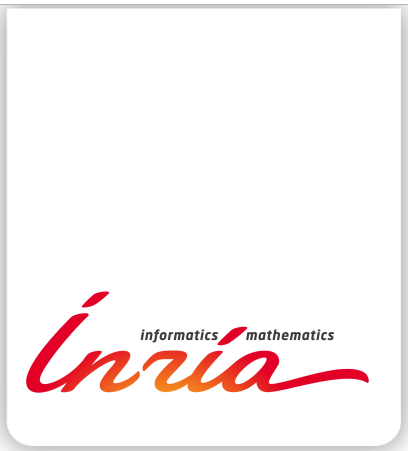

Local Lubrication Model for Spherical Particles within an Incompressible Navier-Stokes Flow

Baptiste Lambert*†, Lisl Weynans†‡, Michel Bergmann†‡

Project-Teams Memphis

Research Report n° 9093 — version 2 — initial version September 2017 — revised version Janvier 2018 — 33 pages

Abstract: The lubrication effects are short-range hydrodynamic interactions essential to the suspension of the particles, and are usually underestimated by direct numerical simulations of particle laden flows. In this paper, we propose a lubrication model for a coupled volume penalization method and discrete element method solver which estimates the unresolved hydrodynamic forces and torques in an incompressible Navier-Stokes flow. Corrections are made locally on the surface of the interacting particles without any assumption on the global particle shape. The numerical model has been validated against experimental data and is shown to perform as well as existing numerical models that are limited to spherical particles.

Key-words: Local Lubrication Correction Model, Particle Laden Flow, Direct Numerical Simulations, Coupled VP-DEM

* baptiste.lambert@inria.fr
† Univ. Bordeaux, IMB, UMR 5251, F-33400 Talence, France
‡ CNRS, IMB, UMR 5251, F-33400 Talence, France

RESEARCH CENTRE
BORDEAUX – SUD-OUEST

200 avenue de la Vieille Tour
33405 Talence Cedex

Modèle local de lubrification pour des écoulements Navier-Stokes incompressible de particles sphériques

Résumé : Les forces de lubrifications jouent un rôle fondamental dans le phénomène de suspension de particules solides dans un fluide visqueux. Ces forces hydrodynamiques de courte distance d'action sont généralement partiellement capturées par la résolution numérique directe des équations de l'écoulement. L'objectif de cet article est de proposer un modèle pour corriger localement les forces et moments de lubrification. Les corrections sont faites directement sur les éléments de surfaces des particules où les effets de lubrification sont sous-estimés, sans hypothèse sur la géométrie globale des particules. Le modèle proposé a été testé sur deux cas expérimentaux dans le cas de particules sphériques.

Mots-clés : Modèle local de lubrification, Ecoulement de particles, Intéraction fluide structure

Contents

1 Introduction

Mixtures of solid particles in a liquid, i.e. suspensions, are a type of two-phase flow that appear in various industrial applications as well as in natural flows. For instance, sedimentation in rivers or near-coast has an influence on the flow. By understanding the dynamics of the bed-load transport, the evolution of the river-stream can be forecast to prevent abnormal erosion or obstruction of waterways[1, 2]. Macroscopic suspensions are also relevant in several industrial applications such as nuclear waste processing, water treatment and reinforced plastics manufacturing. For dense mixtures as uncured solid rocket fuel or concretes, a high concentration of solid particles is desired without compromising the rheological properties and the flowing behavior of the mixture.

Along the years, several numerical methods have been developed to simulate particle laden flows at different scales. However, due to the importance of the fluid-particle interactions, only microscale methods are relevant since they fully resolve the flow around each particle. Since the computational cells are larger than the particle size, macroscale methods such as Stokesian Dynamics (SD)[3, 4] or Force-Coupling Method (FCM)[5, 6], cannot capture the essential details of the flow. Both methods depend on a truncated multipole expansion of the Stokes equations. Thereby they are usually suited only for specific particle shapes and are inherently restricted to non inertial flows. From the limitations of macroscale methods, Direct Numerical Simulation (DNS) has emerged as an appealing alternative, reachable thanks to modern improvements of computer performances. By solving the governing equations (Navier-Stokes equations) directly without any further assumptions, DNS enables microscale simulations of arbitrary particle shape at the numerical method accuracy level. The DNS methods can be divided into two classes. The first class considers boundary-fitted approach[7, 8] where the fluid fills the meshed domain. As

long as the mesh elements are small enough, this approach enables an accurate computation of the boundary layers and interactions between particles. However, as the particles move, the domain needs to be constantly adapted leading to complex and expansive remeshing issues. The computational cost of the remeshing limits three dimensional simulations to about a hundred of particles[8]. In contrast, the second class of DNS methods considers non-boundary-fitted meshes which are more suited to numerical simulations using a large number of particles. In this approach, the whole domain is discretized on an Eulerian fixed grid where the particles are embedded. Several techniques are available to simulate the particulate flow using fictitious domain methods[9, 10, 11, 12, 13, 14, 15], encompassing lattice Boltzmann methods[16], immersed boundary methods (IBM)[17, 18] and volume penalization method (VP)[19]. In this paper, numerical simulations have been performed using a VP approach coupled with a Discrete Element Method (DEM)[¯11]. This last is widely used for granular flow simulation. In this fully coupled method, the particles are tracked using Lagrangian markers. The particle dynamics are solved using the Newton's laws.

Although microscale methods are able to capture flow details, they are challenged by some short range effects. As two particles are moving toward each other they start to interact throughout the fluid as the separation distance $a\epsilon$ (where a denotes the particle radius) becomes small. This well known lubrication effect is due to the draining of interstitial fluid in the gap between the two interacting particles. The normal and tangential components of the lubrication force diverge as the particles collide (ϵ tends to 0) as ϵ^{-1} and $\log(\epsilon)$ respectively. At low Reynolds number values, DNS methods should be able to resolve these lubrication forces if the grid spacing is small enough. Typically, the grid spacing should be at least smaller than $10^{-3}a$ to capture lubrication effects[20]. The computational costs make long term simulations of concentrated suspensions prohibitive. Most simulations are performed on meshes with grid spacing of about $10^{-1}a$, meaning that the accuracy of the description of the lubrication effects drops as the particles come in near contact. Therefore a numerical lubrication model is usually introduced to balance the unresolved lubrication forces. The simplest lubrication model consists in adding the theoretical lubrication force known for two spherical particles (normal[21] and tangent[?] components) to the computed hydrodynamic force[22]. This approach considers that lubrication cannot be captured by the flow solver. However, by adding the theoretical lubrication force, the lubrication partially captured by the solver is counted twice. A more accurate approach is suggested in Stokesian Dynamics, where hydrodynamic forces are split into a long- and a short-range actions. The short-range actions are also known as lubrication. Hence long-range actions are provided by the solver and short-range actions are modeled via the lubrication theory, avoiding an overestimation of the total hydrodynamic forces. However, this decomposition is not easy to adapt to DNS since the long-range hydrodynamics is not explicitly known. A common technique[20, 23] is to perform off-line simulations of two isolated particles using a refined mesh without any lubrication model, for different configurations and the normalized separation distance ϵ, in order to estimate the unresolved part of the lubrication forces. From these off-line simulations and the lubrication theory, a tabulation of lubrication corrections is created. Hence the lubrication model for on-line simulations estimates the correction to perform from the tabulation. The accuracy of this method depends on the quality of the tabulation and the diversity of the off-line samples used to create it. Thus these methods are usually used for monodisperse suspensions of spherical particles since the tabulation of a single parameter is only required. Theoretically, the tabulation of more generals suspensions is also possible[?]. However, the computation cost involved to generate an accurate tabulation depending on several parameters makes generals suspensions unachievable in reasonable CPU time.

In this paper, a lubrication model for incompressible Navier-Stokes flows without tabulation is proposed. The main key-point of our model is a local correction of the lubrication effects

on the particle surface without any assumption on the particle global geometry. This article is organized as follows. In section 2, we present the theoretical background of our model based on a similar framework than the lubrication theory. Section 3 briefly introduces the soft sphere model developed by Walton *et al.*[24] for particle collisions. Section 4 details the numerical method used to solve the particle laden flow. Finally, our local lubrication correction model is validated using two experimental cases in the section 5.

2 Theoretical Framework for lubrication model

The local lubrication correction model developed in this paper is based on a theoretical framework used in the classical lubrication theory [21, ?]. Furthermore, the analytic expression of the local lubrication forces and torques have been obtained using the same methodology as used in the lubrication theory. Therefore, the reader will be referred to the original references for mathematical calculations that are identical to the lubrication theory.

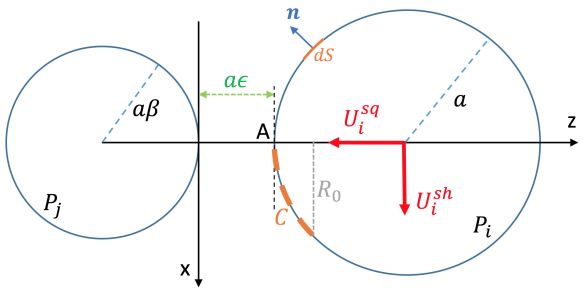

Figure 1: Sketch of two particles in interaction.

2.1 Squeezing Motion of Rigid Spheres

Two smooth particles of radii a and βa (with $\beta > 0$) immersed in an infinite fluid domain are considered. One of the particle (P_i) is moving at the constant velocity $\mathbf{U}_i = -U_i^{\mathrm{sq}}\mathbf{e_z}$ toward the second stationary particle (P_j) (figure 1).The surfaces of P_i and P_j are denoted respectively Γ_i and Γ_j. The gap between the two particles is denoted $a\epsilon$ with $0 < \epsilon \ll 1$.

We consider the flow in the gap in the neighborhood of the contact point A, such that the Reynolds number in the gap is small ($Re = \rho U_i^{\mathrm{sq}} a\epsilon/\mu \ll 1$). Hence, the flow can be modeled by the Stokes equations (1):

$$\left\{\begin{array}{rcl} \mu\Delta\mathbf{u} & = & \nabla p, \\ \nabla\cdot\mathbf{u} & = & 0, \\ \mathbf{u}\restriction_{\Gamma_i} & = & \mathbf{U}\restriction_{\Gamma_i}, \\ \mathbf{u}\restriction_{\Gamma_j} & = & \mathbf{U}\restriction_{\Gamma_j}, \\ \lim\limits_{r\to+\infty} p & = & 0, \end{array}\right. \tag{1}$$

where $\mathbf{u}$ is the velocity field, p is the pressure field, ρ is the fluid density, μ the fluid dynamic viscosity, and the particle surface velocities are $\mathbf{U}\restriction_{\Gamma_i} = -U_i^{\mathrm{sq}}\mathbf{e_z}$ and $\mathbf{U}\restriction_{\Gamma_j} = 0$.

The system (1) is transformed by introducing the Stokes stream-function ψ in the cylindrical coordinate system (r, θ, z) defined such that[25, 26, 27] $(u_r, u_\theta, u_z) = \left(\frac{1}{r}\partial_z\psi, 0, -\frac{1}{r}\partial_r\psi\right)$:

$$\Leftrightarrow \left\{ \begin{array}{rcl} \Phi^4(\psi) & = & 0, \\ \psi \restriction_{\Gamma_i} & = & \frac{1}{2} U_i^{\mathrm{sq}} r^2, \\ \psi \restriction_{\Gamma_j} & = & 0, \end{array} \right. \tag{2}$$

with $\Phi^2(\cdot) = r\partial_r\left(\frac{1}{r}\partial_r(\cdot)\right) + \partial_z^2(\cdot)$. The stream-function ψ solution of (2) can be found near the particle surface Γ_i via the Taylor expansion of ψ as detailed by Jeffrey *et al.*[26]

The lubrication force is due to the hydrodynamic effect of the interaction of the given particle with a nearby obstacle. Thereby, the force is given by the action of the fluid stress on a particle surface when this particle and the interacting obstacle are isolated in an unbounded domain (flow field at rest far from the particles). The lubrication force is directly obtained by integrating the fluid stress σ acting on the particle surface.

$$\sigma = -pI + \mu\left(\nabla\mathbf{u} + (\nabla\mathbf{u})'\right), \tag{3}$$

with I the identity matrix.

Due to the symmetry of the flow, only the stress induced by a force acting parallel to the axis of revolution (Oz) is relevant. Thus the lubrication force on P_i is:

$$\mathbf{F}_i^{\mathrm{lub}} = \left(\int_{\Gamma_i} (\sigma\cdot\mathbf{n})\cdot\mathbf{e_z}\, dS\right)\mathbf{e_z}, \tag{4}$$

with $\mathbf{n}$ the outgoing unit vector of the surface element dS of the particle P_i as shown figure 1.

In any plan containing the axe (Oz), the particle surfaces Γ_i and Γ_j can be characterized, near the contact point, as follows:

$$\left\{ \begin{array}{rcll} z_i(r) & = & a(1+\epsilon) - \sqrt{a^2 - r^2} & \sim \quad a\epsilon + \dfrac{r^2}{2a} + O\left(r^4\right) \\ z_j(r) & = & -\beta a + \sqrt{\beta^2 a^2 - r^2} & \sim \quad -\dfrac{r^2}{2\beta a} + O\left(r^4\right) \end{array} \right. \tag{5}$$

To simplify expressions, the "stretched" coordinates are introduced:

$$\left\{ \begin{array}{rcl} R & = & \dfrac{r}{a\sqrt{\epsilon}}, \\ Z & = & \dfrac{z}{a\epsilon}, \\ H & = & Z_i - Z_j = 1 + \dfrac{1+\beta}{2\beta}R^2 + O(\epsilon), \end{array} \right. \tag{6}$$

where Z_i and Z_j are respectively $z_i(r)$ and $z_j(r)$ from (5) in the "stretched" coordinates.

Via straightforward calculations and simplifications detailed by Happel *et al.*[28], the lubrication force on the particle P_i is expressed as a function of ψ, solution of (2), as follows:

$$\mathbf{F}_i^{\mathrm{lub}} = \pi\mu\int_C r^3\partial_n\left(\frac{\Phi^2(\psi)}{r^2}\right) ds\, \mathbf{e_z}, \tag{7}$$

where $ds = \sqrt{\epsilon}\left(1 + \frac{1}{2}\epsilon R^2\right) dR + O\left(\epsilon^{3/2}\right)$ and $\partial_n = -\epsilon^{-1}\partial_Z + \frac{1}{2}R^2\partial_Z + R\partial_R + O(\epsilon)$ in the "stretched" coordinates[25, 26, 28] (6). The "inner" region, where the solution ψ of (2), is defined by the neighborhood $C = [0, R_0]$ of the contact point A (see figure 1).

Therefore the dominant order (in ϵ) of the lubrication force in the "inner" region is given by:

$$\frac{\mathbf{F}_i^{\text{lub,in}}}{\pi\mu a U_i^{\text{sq}}} = -\frac{6R_0^4}{4H_0^2}\,\frac{1}{\epsilon}\mathbf{e_z} + O(1)\,. \tag{8}$$

To obtain the lubrication force on the whole surface, the lubrication force on the "outer" region needs to be added to the contribution from the "inner" region (8). This can be done by solving (7) with ψ solution of a Stokes problem in the "outer" region and matching this solution to the solution in the "inner" region[26]. Another approach is to match the "inner" solution (8) with a solution on the "outer" region obtained via a detailed numerical simulation[25]. At the end, both methods give the dominant order of the total lubrication force as follows:

$$\frac{\mathbf{F}_i^{\text{lub}}}{\pi\mu a U_i^{\text{sq}}} = -\frac{6}{\epsilon}\mathbf{e_z} + O(1)\,. \tag{9}$$

2.2 Shearing Motion of Rigid Spheres

As for the squeezing motion, two smooth particles of radii a and βa, with $\beta > 0$, are immersed in an infinite domain of fluid. The particle P_i is now moving near the stationary particle P_j at the velocity $\mathbf{U}_i = U_i^{\text{sh}}\mathbf{e_x}$ (see figure 1). The surfaces of P_i and P_j are denoted respectively Γ_i and Γ_j. The gap between the two particles is denoted by $a\epsilon$ ($0 < \epsilon \ll 1$) such as the gap Reynolds number is small ($Re = \rho U_i^{\text{sh}} a\epsilon/\mu \ll 1$).

According to Kim *et al.*[25], symmetries in the flow field in the gap suggest that $(\mathbf{u}, p)$ can be written in the cylindrical coordinate system $(\mathbf{e_r}, \mathbf{e}_\theta, \mathbf{e_z})$ as follows:

$$\left\{\begin{array}{rcl} u_r &=& U_i^{\text{sh}} U(r,z)\cos(\theta)\,,\\ u_\theta &=& U_i^{\text{sh}} V(r,z)\sin(\theta)\,,\\ u_z &=& U_i^{\text{sh}} W(r,z)\cos(\theta)\,,\\ p &=& \dfrac{\mu U_i^{\text{sh}}}{a} P(r,z)\cos(\theta)\,, \end{array}\right. \tag{10}$$

where the angle θ defined such that $\mathbf{e_r} = \cos(\theta)\mathbf{e_x} + \sin(\theta)\mathbf{e_y}$, and U, V, W, and P are unknown functions such that the velocity and pressure fields are solutions of the Stokes problem (1). Via regular expansion of U, V, W, and P and the Taylor expansion of $\mathbf{u}$ and p at the particle surface Γ_i, the dominant order (in ϵ) of $(\mathbf{u}, p)$ solution of (1) can be found as detailed by O'Neill *et al.*[?]. In particular, the dominant orders of U, V and P such that $(\mathbf{u}, p)$ is solution of (1), with the particle surface velocities $\mathbf{U}\restriction_{\Gamma_i} = U_i^{\text{sh}}\mathbf{e_x}$ and $\mathbf{U}\restriction_{\Gamma_j} = 0$, are:

$$\left\{\begin{array}{rcl} U_0(R,Z) &=& -\dfrac{1}{2}\dfrac{dP_0}{dR}(Z-Z_j)(Z_i-Z) + \dfrac{Z-Z_j}{H},\\ P_0(R) &=& \dfrac{6R}{5H^2}\left(1-\dfrac{1}{\beta}\right),\\ V_0(R,Z) &=& -\dfrac{1}{2}\dfrac{P_0}{R}(Z-Z_j)(Z_i-Z) - \dfrac{Z-Z_j}{H}, \end{array}\right. \tag{11}$$

in the "stretched" coordinates (6).

As for the squeezing motion, the lubrication force and torque are directly obtained by integration of the fluid stress σ (see (3)) over the particle surface Γ_i. Due to the symmetry of the

flow, only the component of the force according to the (Ox) is non zero. Hence, the lubrication shear force and torque acting on an element of surface dS of Γ_i, are given by:

$$\begin{cases} \mathbf{F}_i^{\text{lub}} = \left(\int_{\Gamma_i} (\sigma \cdot \mathbf{n}) \cdot \mathbf{e_x} \, dS \right) \mathbf{e_x}, \\ \mathbf{T}_i^{\text{lub}} = \int_{\Gamma_i} (\sigma \cdot \mathbf{n}) \wedge \mathbf{e_y} \, dS. \end{cases} \tag{12}$$

By substitution of $(\mathbf{u}, p)$, expressed as (10), solution of the Stokes equation (1), the dominant orders (in ϵ) of the lubrication force and torque in the "inner" region are found:

$$\frac{F_i^{\text{lub,in}}}{a\mu\pi U_i^{\text{sh}}} = \int_0^{R_0} \left[-P_0 R + \partial_Z V_0 - \partial_Z U_0 \right] R dR \, \mathbf{e_x} + O(\epsilon), \tag{13}$$

$$\frac{T_i^{\text{lub,in}}}{a^2\mu\pi U_i^{\text{sh}}} = \int_0^{R_0} \left[\partial_Z U_0 - \partial_Z V_0 \right] R dR \, \mathbf{e_y} + O(\epsilon). \tag{14}$$

3 Collision Model

In a Stokes flow, the contact between obstacles is theoretically impossible due to the lubrication singularity. However, a collision model needs to be considered for physical and numerical purposes.

From a physical perspective, the lubrication effect alone cannot explain some phenomena such as the rebound of particle onto a wall, which occurs at the Stokes number above roughly[22] $St_d = \frac{\rho_{\text{p}} d U_{\text{c}}}{9\mu} \approx 10$, with ρ_{p}, d and U_{c} the particle density, diameter and impact velocity respectively. The collision model is seen here as a "low cost" model to mimic the effect of the particle deformation on its trajectory. Furthermore, real surfaces are never perfectly smooth, meaning that contact can occur at the particle roughness scale or at the lubrication film breakdown scale (when the separation distance is close to fluid particle characteristic size).

From a numerical point of view, a cutoff distance for the lubrication forces is usually introduced to ensure the model stability. This cutoff distance prevents the lubrication force (9) to diverge as the particle collides with an obstacle. A control on the time step in order to avoid contact due to time discretization errors is not an option. Indeed, an adaptive time step would certainly improve the capture of the lubricating effects, but in case of colliding particles at the Stokes number regime $St_d > 10$, the time step would keep decreasing asymptotically to zero. Therefore, a lubrication cutoff distance and a collision model need to be introduced for stable and finite time simulations.

The collision model chosen here is based on the soft-sphere approach used by Costa *et al.*[29]. The deformation of particles during contact is modeled by the overlap between a particle and an obstacle (particle or wall). From the overlap measurement, normal and tangential contact forces are computed using a mass spring-dashpot system and a Coulomb-type threshold for the tangential component. For a given particle P_i, collision forces $\mathbf{F}_i^{\text{coll}}$ and torque $\mathbf{T}_i^{\text{coll}}$ are decomposed as:

$$\begin{cases} \mathbf{F}_i^{\text{coll}} &= \displaystyle\sum_{j \neq i} \mathbf{F}_{i,j} + \mathbf{F}_{i,\text{wall}}, \\ \mathbf{T}_i^{\text{coll}} &= \displaystyle\sum_{j \neq i} \mathbf{T}_{i,j} + \mathbf{T}_{i,\text{wall}}, \end{cases} \tag{15}$$

where $\mathbf{F}_{i,j}$ is the collision force of the interacting particles P_i and P_j, $\mathbf{F}_{i,\text{wall}}$ is the collision force of P_i with a wall. $\mathbf{T}_{i,j}$ and $\mathbf{T}_{i,\text{wall}}$ are the corresponding collision torques. The force and the

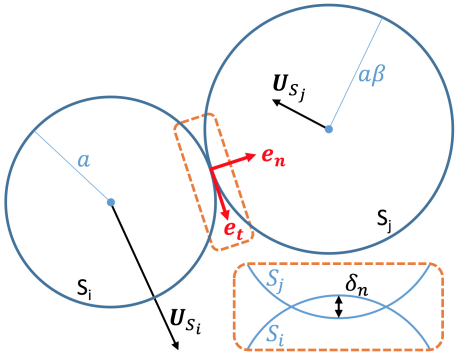

Figure 2: Contact of two particles with notations associated to the soft sphere model.

torque on P_i resulting from the particle-particle interactions between P_i and P_j are defined (as follows) using a local system of coordinates $(\mathbf{e_n}, \mathbf{e_t})$ (figure 2):

$$\left\{ \begin{array}{rcl} \mathbf{F}_{i,j} & = & \mathbf{F}_n + \mathbf{F}_t, \\ \mathbf{T}_{i,j} & = & a\mathbf{e_n} \wedge (\mathbf{F}_t)\,, \end{array} \right. \tag{16}$$

with

$$\left\{ \begin{array}{rcl} \mathbf{F}_n & = & -\boldsymbol{\delta_n} k_{\mathrm{n}} - \gamma_{\mathrm{n}} \left(\mathbf{U}_{i,j} \cdot \mathbf{e_n}\right) \mathbf{e_n}, \\ \mathbf{F}_t & = & \min\left(\| -\boldsymbol{\delta_t} k_{\mathrm{t}} - \gamma_{\mathrm{t}} \left(\mathbf{U}_{i,j} \cdot \mathbf{e_t}\right) \mathbf{e_t} \|, \|\mu_c \mathbf{F}_n\|\right) \mathbf{e_t}, \end{array} \right. \tag{17}$$

where a is the radius of P_i, $\boldsymbol{\delta_n}$ (*resp.* $\boldsymbol{\delta_t}$) is the normal (*resp.* tangential) overlap, k_{n} (*resp.* k_{t}) is the normal (*resp.* tangential) stiffness, μ_c is the friction coefficient, and γ_{n} (*resp.* γ_{t}) is the normal (*resp.* tangential) damping coefficient of the spring-dashpot model. The relative velocity of the two particles $\mathbf{U}_{i,j}$ at the contact point is given by $\mathbf{U}_{i,j} = \mathbf{U}_i + a\omega_i \wedge \mathbf{e_n} - (\mathbf{U}_j - a\beta\omega_j \wedge \mathbf{e_n})$.

The normal overlap distance $\boldsymbol{\delta_n}$ is given by

$$\boldsymbol{\delta_n} = \max\left(0, a\left(1+\beta\right) + \epsilon_{\mathrm{col}}\left(a + \beta a\right) - \|\mathbf{X}_i - \mathbf{X}_j\|\right) \mathbf{e_n}, \tag{18}$$

with $\mathbf{e_n} = \frac{\mathbf{X}_i - \mathbf{X}_j}{\|\mathbf{X}_i - \mathbf{X}_j\|}$ as shown figure 2. The tangential overlap distance $\boldsymbol{\delta_t}$ is obtained by integrating the relative tangential velocity at the point of contact while the Coulomb's law is verified. Therefore the tangential overlap distance ${\boldsymbol{\delta_t}}^{n+1}$ at the time step "$n+1$" is obtained by

$${\boldsymbol{\delta_t}}^{n+1} = \frac{1}{k_{\mathrm{t}}} \left(-\mu_c \|\mathbf{F}_n\| \mathbf{e_t} - \gamma_{\mathrm{t}} \left(\mathbf{U}_{i,j} \cdot \mathbf{e_t}\right) \mathbf{e_t}\right), \tag{19}$$

when the particle is sliding (*i.e.* $\|\mathbf{F}_t\| > \mu_{\mathrm{c}} \|\mathbf{F}_n\|$), and by

$${\boldsymbol{\delta_t}}^{n+1} = R_{\delta_t} \cdot {\boldsymbol{\delta_t}}^{n} + \int_{t^n}^{t^{n+1}} \left(\mathbf{U}_{i,j} \cdot \mathbf{e_t}\right) \mathbf{e_t} dt, \tag{20}$$

when the particle is sticking to the obstacle (*i.e.* $\|\mathbf{F}_t\| \leq \mu_{\mathrm{c}} \|\mathbf{F}_n\|$). The rotation tensor R_{δ_t} moves ${\boldsymbol{\delta_t}}^{n}$ to the new local coordinate system at the state "$n+1$", and

$$\mathbf{e_t} = \frac{-\boldsymbol{\delta_t} k_{\mathrm{t}} - \gamma_{\mathrm{t}} \left(\mathbf{U}_{i,j} - \left(\mathbf{U}_{i,j} \cdot \mathbf{e_n}\right) \mathbf{e_n}\right)}{\| -\boldsymbol{\delta_t} k_{\mathrm{t}} - \gamma_{\mathrm{t}} \left(\mathbf{U}_{i,j} - \left(\mathbf{U}_{i,j} \cdot \mathbf{e_n}\right) \mathbf{e_n}\right) \|}$$

.

The parameters of the spring-dashpot model γ_n, γ_t, k_n, and k_t are calculated from the coefficient of normal (*resp.* tangent) restitution $\xi_{\mathrm{max,n}}$ (*resp.* $\xi_{\mathrm{max,t}}$) of "dry" collision and the contact time τ_c, as follows:

$$\begin{cases} k_\mathrm{n} = \dfrac{m^* \left(\pi^2 + \ln^2\left(\xi_{\mathrm{max,n}}\right)\right)}{\tau_\mathrm{c}^2}, \qquad \gamma_\mathrm{n} = -\dfrac{2m^* \ln\left(\xi_{\mathrm{max,n}}\right)}{\tau_\mathrm{c}}, \\ k_\mathrm{t} = \dfrac{m_t^* \left(\pi^2 + \ln^2\left(\xi_{\mathrm{max,t}}\right)\right)}{\tau_\mathrm{c}^2}, \qquad \gamma_\mathrm{t} = -\dfrac{2m_\mathrm{t}^* \ln\left(\xi_{\mathrm{max,t}}\right)}{\tau_\mathrm{c}}, \end{cases} \tag{21}$$

with the effective mass $m^* = \dfrac{m_i m_j}{m_i + m_j}$, and $m_\mathrm{t}^* = m^* \dfrac{K^2}{K^2+1}$, with $K^2 = 2/5$ the normalized radius of gyration for spherical particles.

The characteristic of the elastic properties of the particles are $\xi_{\mathrm{max,n}}$, $\xi_{\mathrm{max,t}}$ and τ_c. As noticed by Izard *et al.*[22], the relation between τ_c and k_n is unusual, but several studies show that the normal stiffness can be underestimated without modification of the dynamics of a dry system. Such assumption allows to reduce the simulation time since the collision characteristic time will be larger than the particle characteristic deformation time.

In order to ensure the stability of the model and the conservation of the momentum, Costa *et al.*[29] advised that the time step of the overall numerical algorithm Δt has to be chosen as a multiple of the contact time τ_c (at least during the collision). This condition guarantees a zero overlap at the end of the collision, and allows the fluid to adapt itself to sudden changes in velocity of the colliding particles.

The force $\mathbf{F}_{i,\mathrm{wall}}$ and the torque $\mathbf{T}_{i,\mathrm{wall}}$ are assumed to be equivalent to the asymptotic case $\beta \to +\infty$ and $m_{P_j} \to +\infty$.

4 Numerical Model

In this section the numerical methods used to solved the fluid as well as the particle dynamics are detailed in the first two sub-sections and summarized in the figure 7. The local lubrication correction model is described in the last sub-section.

4.1 Discretization of the Governing Equations

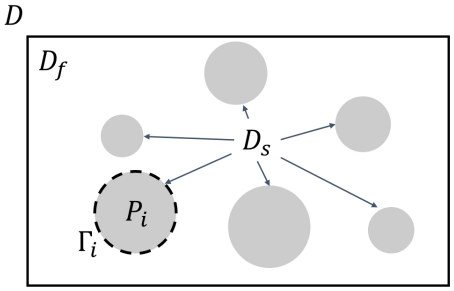

Figure 3: Sketch of the decomposition for the domain D into a fluid domain D_f and the solid particles D_s.

The governing equations considered are the incompressible Navier-Stokes equations for a viscous fluid:

$$\left\{\begin{array}{rcl} \dfrac{\partial u_i}{\partial t}+\dfrac{\partial\left(u_i u_j\right)}{\partial x_j} & = & -\dfrac{1}{\rho}\dfrac{\partial p}{\partial x_i}+\dfrac{\mu}{\rho}\dfrac{\partial}{\partial x_j}\left(\dfrac{\partial u_i}{\partial x_j}\right) \\ & & +\chi\lambda\left(u_{\tau,i}-u_i\right), \\ \dfrac{\partial u_i}{\partial x_i} & = & 0, \end{array}\right. \tag{22}$$

where i; j = 1,2,3, u_i are the velocity components, p is the pressure. The fluid is Newtonian with density ρ and dynamic viscosity μ. The system of equation (22) is solved on an uniform Cartesian mesh of the three dimensional domain $D = D_{\mathrm{f}} \cup D_{\mathrm{s}}$, where N spherical particles P_i forming the solid domain $D_{\mathrm{s}} = \bigcup_{i=1}^{N} P_i$ with $P_i \cap P_j = \emptyset$ for $i \neq j$ and $D_{\mathrm{f}} = D \setminus D_{\mathrm{s}}$ is the fluid domain. The interface between the solid and fluid phases is denoted $\Gamma_{\mathrm{s}} = \bigcup_{i=1}^{N} \Gamma_i$. Each particle P_i is assumed to be homogeneous with a density $\rho_{\mathrm{p},i}$ and a diameter $d_i = 2a_i$.

A non-slip boundary condition is implicitly imposed at the interface Γ_{s}, by the penalty term $\chi\lambda\left(u_{\tau,i}-u_i\right)$. Indeed as reminded by Angot *et al.*[19], solving the penalized equations (22) is equivalent to solve the incompressible Navier-Stokes equations in the fluid domain and to enforce a non-slip boundary condition at the boundary Γ_s, when $\lambda \to +\infty$ and grid element size tends to 0. The computation of the penalty term is detailed later.

The Navier-Stokes equations (22) are discretized using a cell-centered collocated arrangement of the primitive variables (p, u_i). Face-centered velocities v_i are also introduced in addition to the cell-centered velocities u_i, in order to eliminate odd-even decoupling which can lead to large pressure variations in space[30].

The equations are integrated in time using a classical projection scheme introduced by Chorin[31] and Temam[32]. The system (22) is then solved in the following four steps:

1. *Prediction:*
   In this first step, a momentum equation is solved in order to obtained an intermediate virtual velocity u_i^*, starting from a guess for the pressure field q. We choose an incremental scheme so $q = p^n$. The convective and viscous terms are respectively discretized in time by an second-order Adams-Bashforth scheme and an implicit Crank-Nicolson scheme. Hence the following momentum equation (23) is solved at the cell-nodes:

$$\begin{array}{rcl} \dfrac{u_i^*-u_i^n}{\Delta t}+\dfrac{1}{2}\left(3C_i^n-C_i^{n-1}\right) & = & -\dfrac{1}{\rho}\dfrac{\partial q}{\partial x_i} \\ & & +\dfrac{\mu}{2\rho}\left(D_i^*+D_i^n\right) \end{array} \tag{23}$$

   where $C_i = \dfrac{\partial v_j u_i}{\partial x_j}$ and $D_i = \dfrac{\partial}{\partial x_j}\left(\dfrac{\partial u_i}{\partial x_j}\right)$ are respectively the convective and diffusive terms. Spatial derivatives $\frac{\partial}{\partial x}$ are approximated by a second-order central difference. The gradients computed at cell-centers and face-centers are respectively denoted $\left(\frac{\partial}{\partial x_i}\right)_{\mathrm{cc}}$ and $\left(\frac{\partial}{\partial x_i}\right)_{\mathrm{fc}}$.

The virtual face-centered velocities v_i^* are calculated as follows[30]:

$$\left\{\begin{array}{rcl} \hat{u}_i &=& u_i^* + \dfrac{\Delta t}{\rho}\left(\dfrac{\partial q}{\partial x_i}\right)_{\text{cc}}, \\ \hat{v}_1 &=& \gamma_{\text{w}}\hat{u}_{\text{P},1} + (1-\gamma_{\text{w}})\,\hat{u}_{\text{W},1}, \\ \hat{v}_2 &=& \gamma_{\text{s}}\hat{u}_{\text{P},2} + (1-\gamma_{\text{s}})\,\hat{u}_{\text{S},2}, \\ \hat{v}_3 &=& \gamma_{\text{b}}\hat{u}_{\text{P},3} + (1-\gamma_{\text{b}})\,\hat{u}_{\text{B},3}, \\ \hat{v}_i^* &=& \hat{v}_i - \dfrac{\Delta t}{\rho}\left(\dfrac{\partial q}{\partial x_i}\right)_{\text{fc}}, \end{array}\right. \tag{24}$$

where $\hat{\mathbf{u}}_{\text{P}}$, $\hat{\mathbf{u}}_{\text{W}}$, $\hat{\mathbf{u}}_{\text{S}}$, and $\hat{\mathbf{u}}_{\text{B}}$ are velocities computed at the nodes P, W, S, and B respectively (see figure 4). The weights γ_{w}, γ_{s}, and γ_{b} are corresponding to linear interpolation for the west, south and back face velocity components respectively. The same approach is considered for the opposite faces.

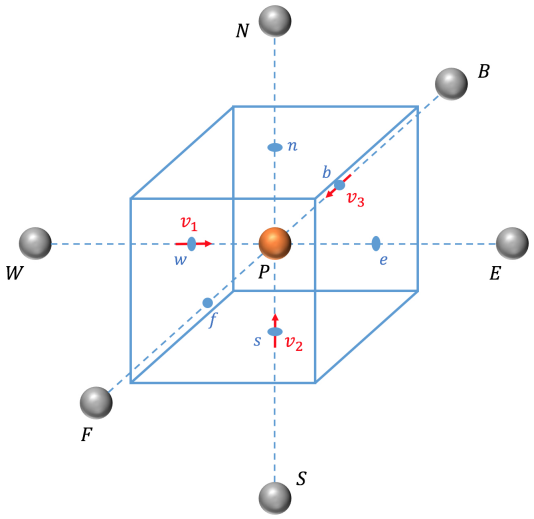

Figure 4: Sketch of a grid cell with the notations used for the spatial discretization of the governing equations.

2. *Projection:*
At the end of projection step, velocities u_i^* are *a priori* not divergence free. The projection step aims to find the pressure field p^{n+1} such that $\nabla \cdot \widetilde{\mathbf{u}} = 0$. In particular, the equation

$$\frac{\widetilde{u}_i - u_i^*}{\Delta t} = \frac{1}{\rho}\frac{\partial p'}{\partial x_i} \tag{25}$$

is solved with the constraint that $\nabla \cdot \widetilde{\mathbf{u}} = 0$. Hence, the following Poisson equation for the pressure correction p':

$$\frac{1}{\rho}\frac{\partial}{\partial x_i}\left(\frac{\partial p'}{\partial x_i}\right) = \frac{1}{\Delta t}\frac{\partial v_i^*}{\partial x_i}, \tag{26}$$

with Neumann boundary conditions on the pressure on all boundaries (of D). Spatial derivatives $\frac{\partial}{\partial x}$ are approximated by a second-order central difference.

The Poisson problem (26) is solved using the Generalized Minimal Residual method (GMRES) developed by Saad *et al.*[33]. Preconditioners are used to reduce the number of iterations needed to ensure a divergence free velocity field, especially for low Reynolds flows.

3. *Correction:*
From the solution p' of the Poisson equation (26) the pressure and velocity fields $\left(p^{n+1}, \widetilde{\mathbf{u}}\right)$ are updated as:

$$\begin{aligned} p^{n+1} &= q + p', \\ \widetilde{u}_i &= u_i^* - \Delta t \frac{1}{\rho} \left(\frac{\partial p'}{\partial x_i}\right)_{\text{cc}}, \\ \widetilde{v}_i &= v_i^* - \Delta t \frac{1}{\rho} \left(\frac{\partial p'}{\partial x_i}\right)_{\text{fc}}, \end{aligned} \tag{27}$$

with $\widetilde{\mathbf{u}}$ is divergence free. Gradients are discretized by second-order central difference. Cell-centers and face-center velocities are updated separately in order to improved the accuracy and stability of the prediction step.

The initial pressure is set arbitrarily to $p^0 = 0$.

4. *Penalization:*
This last step is performed after the resolution of the particle dynamics described in section 4.2 (see figure 7). The velocity field $\widetilde{\mathbf{u}}$ is penalized using the particle velocities $\mathbf{U}^{n+1}$ in order to compute $\mathbf{u}^{n+1}$:

$$u_i^{n+1} = \frac{\widetilde{u}_i + \chi\lambda\Delta t u_{\tau,i}}{1 + \chi\lambda\Delta t}, \tag{28}$$

where λ is the penalty factor (arbitrary chosen in this article such that $\lambda = 10^8$). The characteristic function χ is defined for each cell center location $\mathbf{x}$ such as $\chi(\mathbf{x}) = 1$, if $\mathbf{x} \in D_{\text{s}}$ and the given cell has at least one neighbor in D_{f}. Everywhere else $\chi(\mathbf{x}) = 0$.

The penalization is made using the second-order ghost-cell approach known as Image Point Correction method (IPC)[34]. The main idea of the method is to find the right correction $u_{\tau,i}$ for all solid cells at the fluid-solid interface ($\chi = 1$) in order to impose the desired velocity at the interface Γ_{s}.

The IPC method, illustrated figure 5, corrects the velocity at the solid ghost point G by:

$$\mathbf{u}_\tau = \mathbf{u}_{\text{B}} + \phi \left(\frac{\partial \mathbf{u}}{\partial \mathbf{n}}\right)\Bigg|_{\phi=0}, \tag{29}$$

with $\mathbf{u}_{\text{B}}$ the solid velocity at the surface point B, $\mathbf{n}$ is the outward normal unit vector of the interface. The level set function ϕ is the signed distance from the boundary of the bodies with negative sign within the particles and positive one elsewhere. In particular, $\phi = 0$ at the interface Γ_{s}, and $\|\phi\|$ is the minimal distance to Γ_{s}.

The velocity $\mathbf{u}_{\text{B}}$ can be easily calculated from the velocity $\mathbf{U}$ and rotational velocity $\mathbf{\Omega}$ of the particle mass center. The gradient $(\partial\mathbf{u}/\partial\mathbf{n})|_{\phi=0}$ is determined from $\mathbf{u}_{\text{B}}$ and the velocity $\mathbf{u}_{\text{F}}$ at the symmetric point F of G. The distance between B and F, as well as, the outward normal vector $\mathbf{n}$ can be easily computed with the level set function ϕ.

The velocity at the point F is computed by interpolating the velocities of the eight closest fluid neighbors of F. If one of the eight neighbors is G, the surface point B is considered instead of G. Interpolations are made using a second-order Lagrange interpolation scheme.

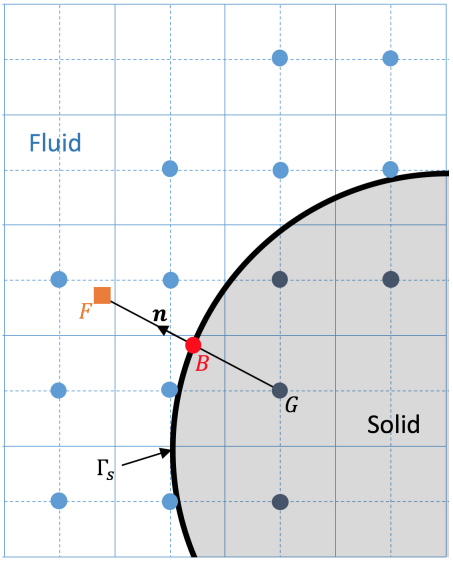

Figure 5: Two-dimensional sketch of the IPC method. Velocity at the solid ghost point G is corrected using its symmetric F. The velocity at F is obtained by interpolation of the velocity of its four neighboring fluid points (eight neighbors in tree-dimensional cases). The orthogonal projection of G at the particle surface is denoted B.

In order to ensure the stability of the whole numerical method, the time step Δt is adapted such that the Courant - Friedrichs - Lewy condition is satisfied: $\Delta t = \beta_\tau \Delta x / V_{\max}$ where $\beta_\tau \leq 1$ is chosen arbitrary, Δx the characteristic length of the grid cells and $V_{\max}$ the maximum of the velocity absolute value computed on the grid cells. However, the time step does not change significantly between to two consecutive iterations. Therefore, the expression of the prediction step (23) is still valid.

When particles are near contact, the time step Δt has to satisfy the stability condition of the collision model. Therefore, when lubrication corrections are active (i.e. collision might occur) Δt is chosen such that $\tau_c = N_t \Delta t$ (with τ_c the contact time) and $\Delta t \leq \beta_\tau \frac{\Delta x}{V_{\max}}$, with $N_t > 0$ an integer ($N_t \geq 8$, in this paper).

4.2 Dynamics of the Particles

The particle dynamics is solved by a discrete element method (DEM) which is primarily devoted to multi-contact interactions for a large suspension[22]. The dynamics of each rigid particle are obtained by the following equations of conservation:

$$m_i \frac{d\mathbf{U}_i}{dt} = \mathbf{F}_i^{\text{hyd}} + \mathbf{F}_i^{\text{coll}} + \mathbf{F}_i^{\text{ext}}, \tag{30}$$

$$\frac{dJ_i \mathbf{\Omega}_i}{dt} = \mathbf{T}_i^{\text{hyd}} + \mathbf{T}_i^{\text{coll}}, \tag{31}$$

for a given particle P_i of mass m_i, inertia matrix J_i, linear velocity $\mathbf{U}_i$ of the mass center and rotational velocity $\mathbf{\Omega}_i$. The hydrodynamic force and torque are respectively denoted $\mathbf{F}_i^{\text{hyd}}$ and

$\mathbf{T}_i^{\text{hyd}}$. Non-hydrodynamic forces like gravity (which is the only external force considered here) are denoted $\mathbf{F}_i^{\text{ext}}$. The force $\mathbf{F}_i^{\text{coll}}$ and torque $\mathbf{T}_i^{\text{coll}}$ represent the effects of solid contacts of P_i with obstacles (see section 3).

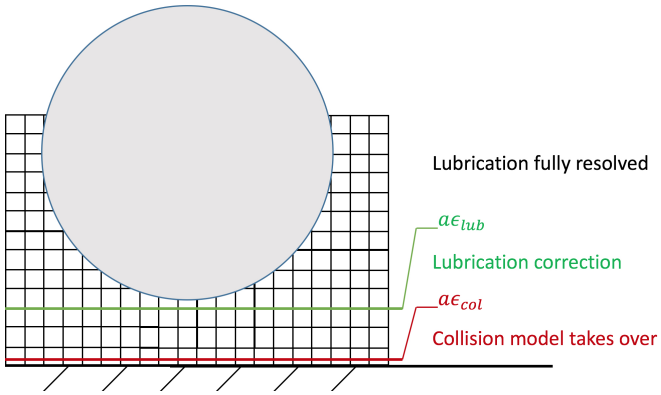

Figure 6: Representation of the two parameters ϵ_{lub} and ϵ_{col} of the lubrication correction model. Typically, $a\epsilon_{\text{lub}} \sim 2-3$ grid cells.

In order to numerically compute the hydrodynamic force and torque, the surface Γ_i of the particle P_i is meshed using $N_{\text{p},i}$ elements. The k-th element of the mesh of Γ_i is denoted P_i^k and s_k is its surface. The set $\boldsymbol{L}(P_i^k)$ is defined as all the particles P_j, $j \neq i$ such that the distance between the surface of P_j and the center of P_i^k is lower than $a\epsilon_{\text{lub}}$. The distance $a\epsilon_{\text{lub}}$ is defined as the narrowest gap width between the center of the P_i^k and a potential nearby obstacle for the solver to fully resolve hydrodynamic interactions (see figure 6).

The total hydrodynamic force and torque on the particle P_i are given by:

$$\left\{\begin{array}{rcl} \mathbf{F}_i^{\text{hyd}} & = & \mathbf{F}_i^{\text{solv}} + \mathbf{F}_i^{\text{deg}}, \\ \mathbf{T}_i^{\text{hyd}} & = & \mathbf{T}_i^{\text{solv}} + \mathbf{T}_i^{\text{deg}}. \end{array}\right. \tag{32}$$

The force $\mathbf{F}_i^{\text{deg}}$ and torque $\mathbf{T}_i^{\text{deg}}$ are defined as:

$$\left\{\begin{array}{rcl} \mathbf{F}_i^{\text{deg}} & = & \displaystyle\int_{\substack{\mathbf{p}\in\Gamma_i, \\ \boldsymbol{L}(\mathbf{p})\neq\varnothing}} (\sigma\cdot\mathbf{n})\ dS, \\ \mathbf{T}_i^{\text{deg}} & = & \displaystyle\int_{\substack{\mathbf{p}\in\Gamma_i, \\ \boldsymbol{L}(\mathbf{p})\neq\varnothing}} a_i\mathbf{n}\wedge(\sigma\cdot\mathbf{n})\ dS. \end{array}\right. \tag{33}$$

These two components of the hydrodynamics are underestimated by the numerical simulation due to the insufficient number of grid elements in the gap between the particle P_i and its surrounding obstacles, to properly capture the fluid flow. Therefore a local lubrication correction model is introduced to balance the degraded hydrodynamics (see section 4.3, below). Lubrication correction on the force and torque are respectively denoted $\mathbf{F}_i^{\text{lub}}$ and $\mathbf{T}_i^{\text{lub}}$.

The remaining of the hydrodynamics, $\mathbf{F}_i^{\text{solv}}$ and $\mathbf{T}_i^{\text{solv}}$ are obtained via the flow solver, as follows:

$$\left\{\begin{array}{rcl} \mathbf{F}_i^{\text{solv}} & = & \displaystyle\int_{\substack{\mathbf{p}\in\Gamma_i, \\ \boldsymbol{L}(\mathbf{p})=\varnothing}} (\sigma\cdot\mathbf{n})\ dS, \\ \mathbf{T}_i^{\text{solv}} & = & \displaystyle\int_{\substack{\mathbf{p}\in\Gamma_i, \\ \boldsymbol{L}(\mathbf{p})=\varnothing}} a_i\mathbf{n}\wedge(\sigma\cdot\mathbf{n})\ dS. \end{array}\right. \tag{34}$$

The resolved hydrodynamics are computed by numerical integration of the fluid stress σ acting on all elements P_i^k far enough to nearby obstacles:

$$\left\{\begin{array}{rcl} \mathbf{F}_i^{\text{solv}} & \approx & \displaystyle\sum_{\substack{k\in[\![1,N_{\text{p},i}]\!],\\ \boldsymbol{L}(P_i^k)=\varnothing}} (\sigma\cdot\mathbf{n})\ s_k, \\ \mathbf{T}_i^{\text{solv}} & \approx & \displaystyle\sum_{\substack{k\in[\![1,N_{\text{p},i}]\!],\\ \boldsymbol{L}(P_i^k)=\varnothing}} a_i\mathbf{n}\wedge(\sigma\cdot\mathbf{n})\ s_k, \end{array}\right. \tag{35}$$

The fluid stress σ is computed, at the center of P_i^k, by interpolation of the pressure and velocities $(p,\mathbf{u}_i)$ solved on the eight neighbouring grid cells. Interpolations are made using a second-order Lagrange scheme.

Among the forces acting on the particle, the short-range hydrodynamics (lubrication) and collision forces have time scales smaller than the time scale associated to fluid flow. The particle dynamics is therefore computed at a smaller time step $\delta t=\frac{\Delta t}{n_t}$, with n_t arbitrary chosen large, in order to accurately integrate (in time) short-range interaction forces. Numerical simulations have shown that changing n_t between 10^2 and 10^3 does not affect significantly the results. Since the motion of the particles occurs at a time step smaller than Δt, it is not necessary to re-compute the resolved hydrodynamic forces $\mathbf{F}_i^{\text{solv}}$ at each sub-time step δt. Hence, particle dynamics is solved at each sub-time step δt with updated short-range interactions and "frozen" resolved hydrodynamics. The discretized expressions of (30) and (31) are then written as:

$$\begin{array}{rcl} \mathbf{U}_i^{m+1} & = & \mathbf{U}_i^m+\dfrac{\delta t}{m_i}\left[\mathbf{F}_i^{\text{solv}}\right]^{n+1} \\ & & +\dfrac{\delta t}{m_i}\left[\mathbf{F}_i^{\text{coll}}+\mathbf{F}_i^{\text{ext}}+\mathbf{F}_i^{\text{lub}}\right]^m. \end{array} \tag{36}$$

$$\begin{array}{rcl} \boldsymbol{\Omega}_i^{m+1} & = & \left(J_i^{m+1}\right)^{-1}\left(J_i^m\boldsymbol{\Omega}_i^m\right. \\ & & \left.+\delta t\left(\left[\mathbf{T}_i^{\text{solv}}\right]^{n+1}+\left[\mathbf{T}_i^{\text{coll}}+\mathbf{T}_i^{\text{lub}}\right]^m\right)\right), \end{array} \tag{37}$$

where m denotes the "sub-state" of the system at the time $t=t_n+m\delta t$ with t_n the time at the state n of the system. Since the particle dynamics is solved after the correction step but before the penalization (see figure 7), the force $\left[\mathbf{F}_i^{\text{solv}}\right]^{n+1}$ and torques $\left[\mathbf{T}_i^{\text{solv}}\right]^{n+1}$ are computed from the fields $\left(p^{n+1},\widetilde{\mathbf{u}}\right)$, and not $\left(p^{n+1},\mathbf{u}^{n+1}\right)$.

4.3 The Local Lubrication Correction Model

The lubrication force $\mathbf{F}_i^{\text{lub}}$ and torque $\mathbf{T}_i^{\text{lub}}$ acting on P_i are given by:

$$\begin{array}{rcl} \mathbf{F}_i^{\text{lub}} & = & \displaystyle\sum_{j\in[\![1,N]\!]\setminus\{i\}} \mathbf{F}_{i,j}^{\text{lub}}+\mathbf{F}_{i,\text{wall}}^{\text{lub}}, \\ \mathbf{T}_i^{\text{lub}} & = & \displaystyle\sum_{j\in[\![1,N]\!]\setminus\{i\}} \mathbf{T}_{i,j}^{\text{lub}}+\mathbf{T}_{i,\text{wall}}^{\text{lub}}, \end{array} \tag{38}$$

where $\mathbf{F}_{i,j}^{\text{lub}}$ and $\mathbf{T}_{i,j}^{\text{lub}}$ are respectively the lubrication force and torque acting on P_i, created by the interaction of P_i and P_j. The lubrication force and torque created by the interaction of the

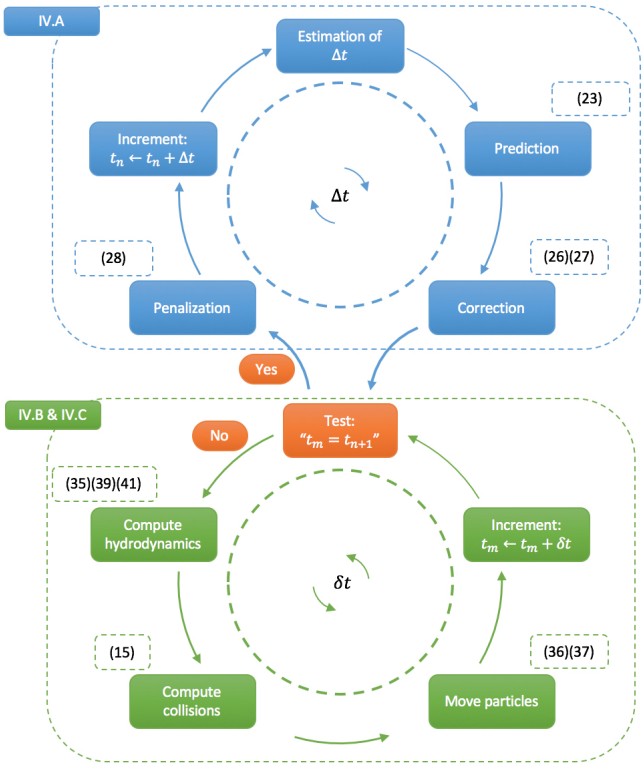

Figure 7: Sketch description of the numerical algorithm used to compute the state $n+1$ of the whole system from its state n. The algorithm starts at the estimation of the time step Δt which is the time elapse between the system state n and $n+1$. The particle dynamics is solved in n_t sub-time steps $\delta t = \frac{\Delta t}{n_t}$. m denotes the current sub-state of the system between the state n and $n+1$ while the particle dynamics is computed (NB: after the step "correction", the state m is equivalent to the state n). Dashed boxes contains the reference to the main equations computed at the given step.

particle P_i with a wall are denoted respectively $\mathbf{F}^{\text{lub}}_{i,\text{wall}}$ and $\mathbf{T}^{\text{lub}}_{i,\text{wall}}$, and are equivalent to the asymptotic case $\beta \to +\infty$.

From the lubrication theory detailed in section 2, $\mathbf{F}^{\text{lub}}_{i,j}$ and $\mathbf{T}^{\text{lub}}_{i,j}$ are given by:

$$\left\{\begin{array}{lcl}
\mathbf{F}^{\text{lub}}_{i,j} & = & \left(\mathbf{F}^{\text{lub,sq}}_{i,j} + \mathbf{F}^{\text{lub,sh}}_{i,j}\right) 1_{[\epsilon_{\text{lub}},\epsilon_{\text{col}}]}(\epsilon), \\
\mathbf{T}^{\text{lub}}_{i,j} & = & \mathbf{T}^{\text{lub,sh}}_{i,j}\, 1_{[\epsilon_{\text{lub}},\epsilon_{\text{col}}]}(\epsilon), \\
\dfrac{\mathbf{F}^{\text{lub,sq}}_{i,j}}{\pi\mu a U^{\text{sq}}_{i,j}} & = & -\dfrac{6R_0^4}{4H_0^2}\dfrac{1}{\epsilon}\,\mathbf{e_n}, \\
\dfrac{\mathbf{F}^{\text{lub,sh}}_{i,j}}{\pi\mu a U^{\text{sh}}_{i,j}} & = & \int_0^{R_0}\left[-P_0 R + \partial_Z V_0 - \partial_Z U_0\right] R dR\,\mathbf{e_t}, \\
\dfrac{\mathbf{T}^{\text{lub,sh}}_{i,j}}{\pi\mu a^2 U^{\text{sh}}_{i,j}} & = & \int_0^{R_0}\left[\partial_Z U_0 - \partial_Z V_0\right] R dR\,\mathbf{e_n}\wedge\mathbf{e_t}, \\
U^{\text{sq}}_{i,j} & = & U^{\text{sq}}_i - U^{\text{sq}}_j, \\
U^{\text{sh}}_{i,j} & = & U^{\text{sh}}_i - U^{\text{sh}}_j + (\omega_i - \omega_j\beta)\,a,
\end{array}\right. \tag{39}$$

with $H_0 = 1 + \frac{1}{2}a\alpha R_0^2$, $\alpha = \frac{\beta+1}{a\beta}$, and $R_0 = \frac{1}{\sqrt{\epsilon}}\sqrt{1-(1+\epsilon-\epsilon_{\text{lub}})^2}$ (see figure 8). The projected relative velocity of the two particles on the direction $\mathbf{e_n}$ and $\mathbf{e_t}$ are respectively $U^{\text{sq}}_{i,j}$ and $U^{\text{sh}}_{i,j}$ (see figure 8).

The indicator function $1_{[\epsilon_{\text{lub}},\epsilon_{\text{col}}]}(\epsilon)$ is non zero and equals to 1 only if $\epsilon_{\text{col}} \le \epsilon \le \epsilon_{\text{lub}}$. Hence the lubrication model is switched off when the hydrodynamics is fully resolved ($\epsilon \ge \epsilon_{\text{lub}}$), and when the gap disappears ($\epsilon \le \epsilon_{\text{col}}$).

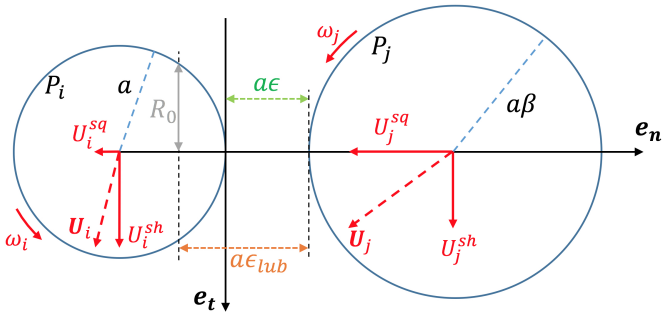

Figure 8: Sketch of the two interacting particles with the notations used to evaluate $\mathbf{F}^{\text{lub}}_{i,j}$ and $\mathbf{T}^{\text{lub}}_{i,j}$.

The analytic expressions of $\mathbf{F}^{\text{lub,sh}}_{i,j}$ and $\mathbf{T}^{\text{lub,sh}}_{i,j}$ are not as simple as the expression of $\mathbf{F}^{\text{lub,sq}}_{i,j}$. Therefore we choose to compute the shearing components by numerical integration. Furthermore, numerical integration will be necessary if we want to add lower orders of the lubrication forces and torques. The force $\mathbf{F}^{\text{lub,sh}}_{i,j}$ and the torque $\mathbf{T}^{\text{lub,sh}}_{i,j}$ are integrated on n_{lub} sub-sets of the lubrication region $[0, R_0]$:

$$\begin{array}{lcl}
\dfrac{\mathbf{F}^{\text{lub,sq}}_{i,j}}{\pi\mu a U^{\text{sq}}_{i,j}} & = & \displaystyle\sum_{k=1}^{n_{\text{lub}}}\int_{\boldsymbol{R}_k}\left[-P_0 R + \partial_Z V_0 - \partial_Z U_0\right] R dR\ \mathbf{e_t}, \\
\dfrac{\mathbf{T}^{\text{lub,sh}}_{i,j}}{\pi\mu a^2 U^{\text{sh}}_{i,j}} & = & \displaystyle\sum_{k=1}^{n_{\text{lub}}}\int_{\boldsymbol{R}_k}\left[\partial_Z U_0 - \partial_Z V_0\right] R dR\ \mathbf{e_n}\wedge\mathbf{e_t},
\end{array} \tag{40}$$

where $\boldsymbol{R}_k = \left[\frac{k-1}{n_{\text{lub}}}R_0, \frac{k}{n_{\text{lub}}}R_0\right]$.

The local lubrication correction model (LLCM) is then built such that the total hydrodynamic force and torque acting on P_i is approximated by:

$$\left\{\begin{array}{lcl} \mathbf{F}_i^{\text{hyd}} & \approx & \mathbf{F}_i^{\text{solv}} + \mathbf{F}_i^{\text{lub}}, \\ \mathbf{T}_i^{\text{hyd}} & \approx & \mathbf{T}_i^{\text{solv}} + \mathbf{T}_i^{\text{lub}}. \end{array}\right. \tag{41}$$

Since lubrication correction $\mathbf{F}_{i,j}^{\text{lub}}$ and $\mathbf{T}_{i,j}^{\text{lub}}$ are the dominant order of the hydrodynamics acting on the "inner" region of P_i, when the flow in the gap is in the Stokes regime (see section 2), $\mathbf{F}_i^{\text{lub}}$ and $\mathbf{T}_i^{\text{lub}}$ are not identical to the degraded hydrodynamics $\mathbf{F}_i^{\text{deg}}$ and $\mathbf{T}_i^{\text{deg}}$. Nevertheless, simulations section 5 below show that the approximation $\mathbf{F}_i^{\text{deg}} \approx \mathbf{F}_i^{\text{lub}}$ can be made as long as the gap Reynolds numbers $Re_{i,j}^{\text{gap}} = \dfrac{\rho a_i \epsilon \|\mathbf{U_i} - \mathbf{U_j}\|}{\mu}$ remains small for all P_j in interaction with P_i, during the simulations. In particular, the Reynolds number Re^{lub} needs to be moderate (typically $Re^{\text{lub}} < 10^3$):

$$Re^{\text{lub}} = \frac{\rho \epsilon_{\text{lub}} Q^{\max}}{\mu}, \tag{42}$$

with $Q^{\max} = \max_t \left(\max_{(i,j)\in[\![1,N]\!]^2} (a_i \|\mathbf{U_i}(t) - \mathbf{U_j}(t)\|) \right)$.

This constraint also underlines the limitation of the LLCM to moderate Reynolds number flows. Indeed, inertia effects of the fluid in the gap are not corrected by the LLCM. Another limitation of the LLCM concerns the many-body interactions, which refers to the hydrodynamics action on a particle generated by two nearby particles in interactions. Since the lubrication correction on P_i is only obtained by summing the corrections of the lubrication effects created by the interaction of P_i with others obstacles P_j (see (38)), the only many-body interactions considered are the ones resolved by the numerical method (included in $\mathbf{F}_i^{\text{solv}}$).

5 Results

The validation of the local lubrication correction model has been made in two steps. First, the correction of the dominant component of the lubrication force ("squeeze motion" 2.1) is validated by considering a single particle falling on a wall. Finally, oblique impact of a single particle on a wall are simulated to validate the corrections of the lubrication force and torque created by a sheared motion of the interstitial fluid.

5.1 Sphere Falling on a Wall

A single particle is immersed in a domain $[4d, 4d, 4d]$, with $d = 2a$ the particle diameter, uniformly meshed with cubic elements of size $\Delta x = \Delta y = \Delta z = hd$. Periodic boundary conditions are considered on the lateral faces of the domain. A no-slip condition is imposed at the top and bottom walls (y constant). Simulations have been performed on a $[8d, 8d, 8d]$ domain (with $h = 1/40$) and have given identical solutions than on the smaller domain. The fluid is initially at rest and the particle is dropped without initial velocity such that the gap size from the bottom wall is given by $a\epsilon_{init}$ as shown figure 9. The gravity field g acts on the y-direction.

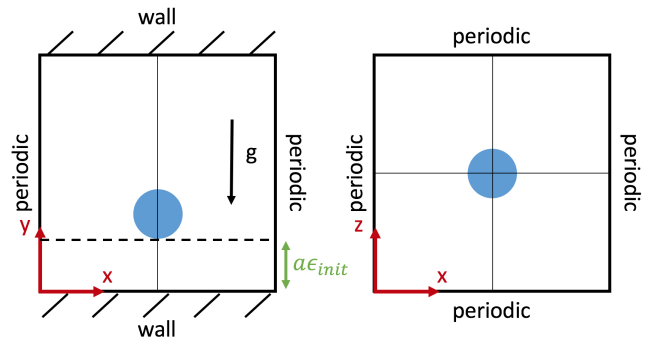

Figure 9: Sketch of two cross sections of the domain with its configuration and initial location of the particle.

In order to have an experimental reference for comparison, we chose the same configuration as one of the two cases from Harada *et al.*[35]. Particle and fluid properties are presented in table 1.

Fluid density	ρ	985	$\mathrm{kg \cdot m^{-3}}$
Fluid dynamic viscosity	μ	0.142	$\mathrm{Pa \cdot s}$
Particle density	ρ_p	1127	$\mathrm{kg \cdot m^{-3}}$
Particle diameter	d	0.0254	m
Normal restitution	$\xi_{\mathrm{max,n}}$	0.97	
Contact time	τ_c	$7.98 \cdot 10^{-5}$	s
Particle roughness	$a\epsilon_\mathrm{col}$	$2 \cdot 10^{-4} d$	m
Gravity field	g	9.781	$\mathrm{N \cdot kg^{-1}}$
Terminal velocity	U_T	0.146	$\mathrm{m \cdot s^{-1}}$
Initial position	ϵ_{init}	0.4181	

Table 1: Simulation configurations.

Under these configurations (table 1), the fluid characteristic Reynolds and Stokes numbers are as follows:

$$\begin{cases} Re_d &= \dfrac{\rho U_T d}{\mu} &\approx 25.7, \\ St_d &= \dfrac{\rho_p U_T d}{9\mu} &\approx 3.27. \end{cases} \tag{43}$$

5.1.1 Comparison with existing lubrication models

Figure 10 compares the particle velocity U simulated using the local lubrication correction model (LLCM) and a tabulated lubrication model (CLM, described bellow) to experimental measurements made by Harada *et al.*[35]. Numerical simulations were performed on an uniform cartesian mesh with a grid spacing $h = 1/40$ and using $N_\mathrm{p} = 3200$ elements for the particle surface mesh. Local lubrication corrections are performed on particle mesh elements closer than $2\Delta y$ to the wall. Numerical experiments have shown that the number of particle surface mesh elements (starting from about a thousand elements) has a limited impact on the solutions. Therefore all

the following simulations have been performed using $N_\mathrm{p} = 3200$ elements for the particle surface mesh.

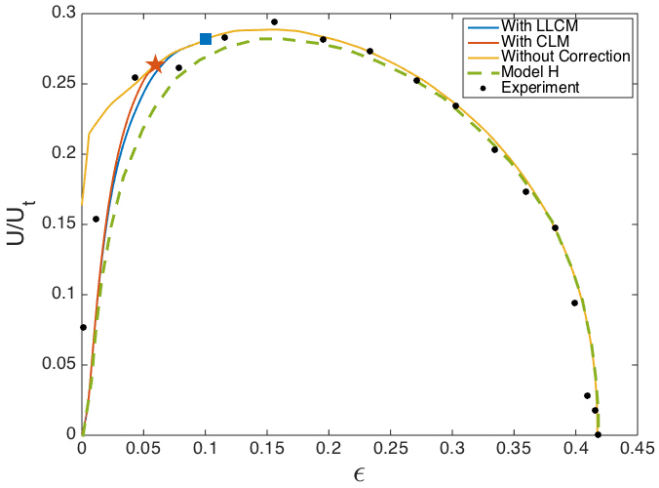

Figure 10: The vertical velocity of the particle in function of the gap non-dimensional size. Simulations using local (LLCM) and tabulated (CLM) lubrication correction are compared to Harada[35] experimental measurements and the model H. The LLCM and CLM are activated for ϵ smaller than respectively the blue square and red star.

The CLM[29] is a two-parameter model which corrects the normal component of the lubrication force on a spherical particle. The correction is made by adding $\Delta\mathbf{F}_i^{\mathrm{lub}} = \Delta F_i^{\mathrm{lub}}\,\mathbf{e_n}$ to the computed hydrodynamic force:

$$\frac{\Delta F_i^{\mathrm{lub}}}{6\pi\mu a U_{i,\mathrm{wall}}^{\mathrm{sq}}} = \begin{cases} \lambda_\mathrm{w}(\epsilon_{\Delta x}) - \lambda_\mathrm{w}(\epsilon), & \epsilon_{\mathrm{col}} \le \epsilon < \epsilon_{\Delta x}, \\ \lambda_\mathrm{w}(\epsilon_{\Delta x}) - \lambda_\mathrm{w}(\epsilon_{\mathrm{col}}), & 0 \le \epsilon < \epsilon_{\mathrm{col}}, \\ 0, & \text{otherwise}, \end{cases} \tag{44}$$

where $\mathbf{e_n}$ is defined as represented figure 8, and λ_w is the Stokes amplification factor for lubrication interaction between a sphere and a wall:

$$\lambda_\mathrm{w}(\epsilon) = \frac{1}{\epsilon} - \frac{1}{5}\ln(\epsilon) - \frac{1}{21}\epsilon\ln(\epsilon) + O(1)\,. \tag{45}$$

Hence, the total hydrodynamic force is given by:

$$\mathbf{F}_i^{\mathrm{hyd}} = \int_{\Gamma_i} (\sigma\cdot\mathbf{n})\,dS + \Delta\mathbf{F}_i^{\mathrm{lub}}. \tag{46}$$

Aside the computation of the hydrodynamics (46), the resolution of the fluid and particle dynamics is identical to the approach used with the LLCM.

The value of the parameter $\epsilon_{\Delta x}$ is determined by simulating the slow approach of a sphere to a wall, for a given grid cell resolution h. Figure 11 represents the total hydrodynamic force acting on a particle approaching a wall. A simulation without lubrication correction is compared to the analytical solution given by Brenner[?]. For $h = 1/40$ the value of $\epsilon_{\Delta x}$ is set to 0.06. Indeed for $\epsilon \le \epsilon_{\Delta x}$ the hydrodynamic force from the simulation without lubrication correction no longer matches the analytical solution[?] (see figure 11).

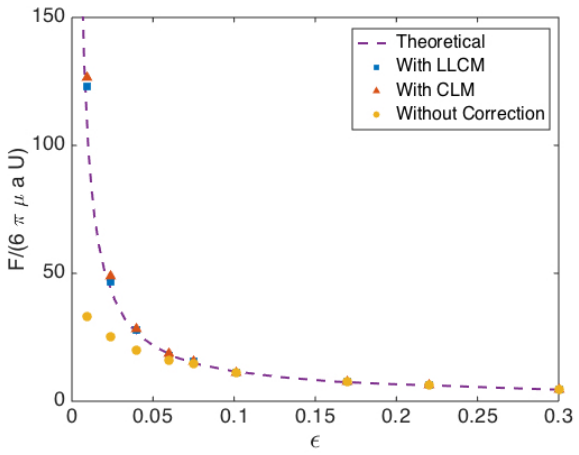

Figure 11: Total hydrodynamic force as a function of ϵ in the case of a single particle approaching a solid wall. Simulations results are compared against the analytical solution of Brenner[?] (dashed line). All simulations are run with $h = 1/40$. The LLCM is activated on all ϵ smaller than $\epsilon_{\text{lub}} = 2\frac{\Delta y}{a}$.

The relative errors L^2 and L^∞ of the particle velocity U obtained by a simulation compared to the experimental particle velocity U_{exp} provided by Harada *et al.*[35] are denoted respectively $E_2(U) = \|U_{\text{exp}} - U\|_2$ and $E_\infty(U) = \|U_{\text{exp}} - U\|_\infty$.

Both simulations using CLM (figure 10 and 11) have been run with $\epsilon_{\Delta x} = 0.06$ and $h = 1/40$. For the Harada case, CLM results are in good agreement with experimental measurement. As shown in figure 10, the Pearson's correlation coefficient is equal to 0.9661, $E_2(U_{\text{CLM}}) = 2.287 \cdot 10^{-3}\ \text{m} \cdot \text{s}^{-1}$, $E_\infty(U_{\text{CLM}}) = 1.229 \cdot 10^{-2}\ \text{m} \cdot \text{s}^{-1}$.

In comparison, the accuracy of the LLCM is comparable to the CLM, with simulated velocities remained close to experimental data (Pearson's correlation coefficient equals to 0.9633, $E_2(U_{\text{LLCM}}) = 2.385 \cdot 10^{-3}\ \text{m} \cdot \text{s}^{-1}$, and $E_\infty(U_{\text{LLCM}}) = 1.232 \cdot 10^{-2}\ \text{m} \cdot \text{s}^{-1}$). The LLCM simulation are about 10% more costly than CLM, without considering the computation cost of the tabulation.

However the computation time of the tabulation needed for the CLM can be significant. Furthermore, the LLCM can be extended to non spherical particle while the CLM will required the tabulation of several parameters at a considerable CPU cost. The computational cost of the tabulation is also a CLM's limitation for polydisperse flow of spherical particles. Therefore, the LLCM is reliable and efficient alternative to tabulated methods for complex flow particles.

Due to the lack of experimental measurements of the total hydrodynamic forces for a falling particle, simulated total hydrodynamic forces are compared to an analytic model ("model H") introduced by Harada *et al.*[35]. The model H is based on the Stokesian dynamic, where hydrodynamic forces $\mathbf{F}_i^{\text{Model\_H}} = \mathbf{F}_i^{\text{hyd}} + \mathbf{F}_i^{\text{lub}}$ on the particle are modeled by the dominant order of the lubrication force $\mathbf{f}_{\text{l}}$, the added-mass force $\mathbf{f}_{\text{a}}$ and the history Basset force $\mathbf{f}_{\text{Ba}}$.

The dominant order of the lubrication force is obtained by integration of the interstitial pressure between the particle and the wall[36]:

$$\mathbf{f}_{\text{l}} = 6\pi\mu a \frac{\mathbf{U}_i^{\text{sq}}}{\epsilon}. \tag{47}$$

As the motion of the particle is unsteady, the added mass force changes near the wall as follows[37][?]:

$$\left\{ \begin{array}{rcl} \mathbf{f}_{\mathrm{a}} & = & m' \dfrac{d\mathbf{U}_i}{dt} + \dfrac{1}{2}\dfrac{dm'}{dt}\mathbf{U}_i, \\ m' & = & \dfrac{2}{3}\pi\rho a^3 \left(1 + \displaystyle\sum_{i=0}^{\infty} \frac{3a^{(i+1)}}{f_0 f_1 ... f_i}\right), \end{array} \right. \tag{48}$$

where f_i is recursively defined such that $f_0 = 2a(\epsilon + 1)$ and $f_i = f_0 - a^2/f_{i-1}$.

The Basset history force for a spherical particle is given by:

$$\mathbf{f}_{\mathrm{Ba}} = 6a^2\sqrt{\pi\rho\mu} \int_{-\infty}^{t} \frac{d\mathbf{U}_i}{dt'} \frac{dt'}{\sqrt{t-t'}}. \tag{49}$$

Hence, the total hydrodynamic force of the model H is $\mathbf{F}_i^{\mathrm{Model\_H}} = \mathbf{f}_{\mathrm{Ba}} + \mathbf{f}_{\mathrm{a}} + \mathbf{f}_{\mathrm{l}}$.

Numerical simulations have shown than simulated velocities using the LLCM tend to experimental measurements as h decreased. Table 2 shows that the order of the numerical method used is closed to a second-order in L^2 and L^∞ on velocity (for $h > 1/40$) when no lubrication corrections are applied. The particle dynamics for $h = 1/20$ is only fully resolved for large ϵ, where the lubrication forces are not dominant. Therefore, errors on the particle position and velocity are unexpectedly small for $h = 1/20$ compared to smaller h. Table 2 also show that the LLCM gives better results than model H for $h < 1/40$, even before any lubrication corrections (for the model H: Pearson's correlation coefficient equals to 0.9418, $E_2(U_{\mathrm{Model\_H}}) = 0.0032\,\mathrm{m}\cdot\mathrm{s}^{-1}$, $E_\infty(U_{\mathrm{Model\_H}}) = 0.0130\,\mathrm{m}\cdot\mathrm{s}^{-1}$).

Velocity

h	$\|U_{1/100} - U_h\|_2$	$\|U_{1/100} - U_h\|_\infty$	order L^2	order L^∞
1/20	$2.13 \cdot 10^{-4}$	$4.74 \cdot 10^{-4}$		
1/40	$3.83 \cdot 10^{-4}$	$6.35 \cdot 10^{-4}$	–	–
1/60	$3.27 \cdot 10^{-4}$	$5.48 \cdot 10^{-4}$	2.04	1.95
1/80	$2.50 \cdot 10^{-4}$	$3.75 \cdot 10^{-4}$	1.73	1.58

Position

h	$\|Y_{1/100} - Y_h\|_2$	$\|Y_{1/100} - Y_h\|_\infty$	order L^2	order L^∞
1/20	$2.07 \cdot 10^{-3}$	$2.08 \cdot 10^{-3}$		
1/40	$7.95 \cdot 10^{-4}$	$8.24 \cdot 10^{-4}$	1.81	1.81
1/60	$3.64 \cdot 10^{-4}$	$3.90 \cdot 10^{-4}$	1.62	1.62
1/80	$1.44 \cdot 10^{-4}$	$1.64 \cdot 10^{-4}$	1.54	1.53

Table 2: Table of convergence for the particle position and velocity, when the particle dynamics is fully resolved. The particle position Y_h and velocity U_h obtained with a grid mesh resolution h are compared to the particle position $Y_{1/100}$ and velocity $U_{1/100}$ obtained with a grid mesh resolution $h = 1/100$. The units of the position and velocity errors are respectively m and $\mathrm{m}\cdot\mathrm{s}^{-1}$.

5.1.2 Grid sensitivity analysis

Using the same configuration described in table 1, simulations have been performed with four different background grid resolutions $h = 1/20$, $h = 1/40$, $h = 1/80$ and $h = 1/100$. The total

hydrodynamic forces obtained are compared to the model H (Figure 12).

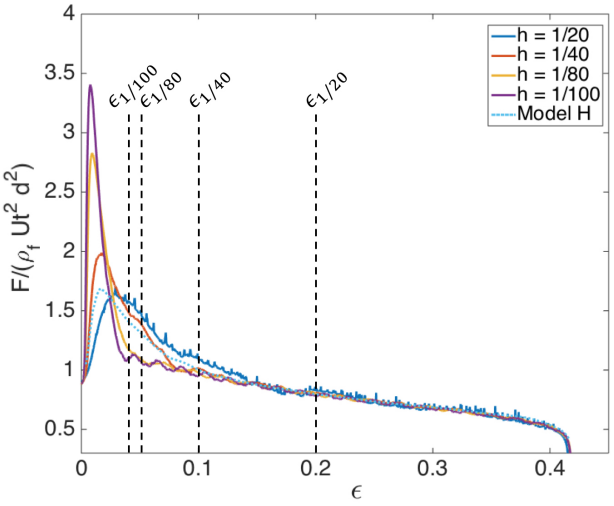

Figure 12: Total hydrodynamic force, according to the y-direction as a function of $1/\epsilon$ during the approach phase. For each grid mesh resolution h, lubrication correction is activated for $\epsilon \leq \epsilon_h$.

Far from the wall ($\epsilon > 0.1$), higher grid resolutions ($h \leq 1/80$) improve the capture of the total hydrodynamic forces. Indeed as shown on the figure 12, the hydrodynamic forces tend to the hydrodynamic force of the model H which fits experimental velocities (figure 10). As the particle goes closer to the wall ($\epsilon < 0.1$), simulated hydrodynamic forces are lower than the solution of the model H, even before any lubrication correction is applied (see $h = 1/80$ and $h = 1/100$). Starting from the same initial conditions, the lower hydrodynamic forces induce higher particle velocities (than model H velocities) close to the wall. Therefore, the response of the LLCM is stronger close to the wall with steeper hydrodynamic force than with the model H. However, the relevance of the model H as reference for $\epsilon < 0.1$ can be discussed since velocities of the model H do not perfectly fit experimental measurements in this range of ϵ (figure 10). As shown on figure 12, the LLCM has a lower hydrodynamic force compare to the model H. However, the particle velocity of the model H for $\epsilon < 0.1$ (figure 10) is lower than experimental data which implies that the model H overestimates the hydrodynamics when $\epsilon < 0.1$.

In order to assess the global rate of convergence of the LLCM, simulations have been performed with different background grid resolutions h and with $\epsilon_{\text{lub}} = 0.1$ fixed. The total hydrodynamic forces obtained are compared to the model H (Figure 13).

The figure 14 shows that the global order of the numerical method used is first-order in L^2 and L^∞ on position and velocity. However, one of the main features of the LLCM, which is to rely as much as possible on the solved fluid stress to compute the hydrodynamics, is ignored for the simulations using finer grid mesh resolution than $h = 1/40$. Therefore the global order of convergence on velocity and position of the LLCM could be closer to a second-order, since the computation of the hydrodynamics rely more and more (as h decrease) on a numerical method without lubrication correction, which is an second-order of converge on position and velocity (see table 2). In addition, the LLCM is more accurate if ϵ_{lub} is adapted to the grid resolution h than if ϵ_{lub} is fixed. For instance with $h = 1/100$, the relative errors $E_2(U_{\text{LLCM}})$ and $E_\infty(U_{\text{LLCM}})$ are increased respectively by 18.7% and 11.8% by using $\epsilon_{\text{lub}} = 0.1$ instead of $\epsilon_{\text{lub}} = \frac{2\Delta y}{a} (= 0.04)$.

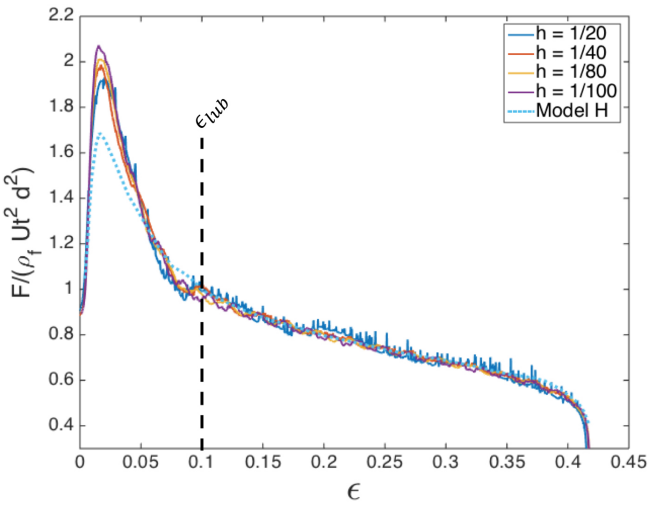

Figure 13: Total hydrodynamic force, according to the y-direction as a function of $1/\epsilon$ during the approach phase. For all curves, lubrication correction is activated for $\epsilon \leq \epsilon_{\text{lub}}$.

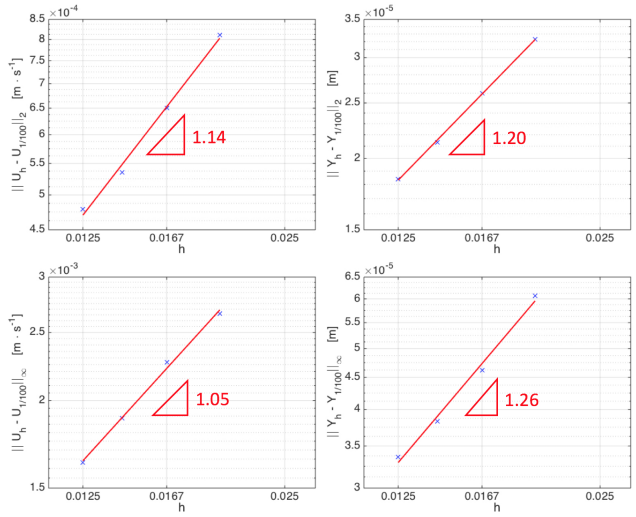

Figure 14: Representation of the global rate of convergence on position (on the right) and velocity (on the left) of the particle center of gravity according to the norms L^2 (top) and L^∞ (bottom). The particle position Y_h and velocity U_h obtained with a grid mesh resolution h are compared to the particle position $Y_{1/100}$ obtained with a grid mesh resolution $h = 1/100$.

5.1.3 Sensitivity analysis from the lubrication parameter ϵ_{lub}

The LLCM is a model with a single parameter ϵ_{lub} which sets the minimum gap length where lubrication corrections are needed. Several simulations have been made for different ϵ_{lub}. Figure 15 represents the total hydrodynamic force normalized by the particle velocity in respect with

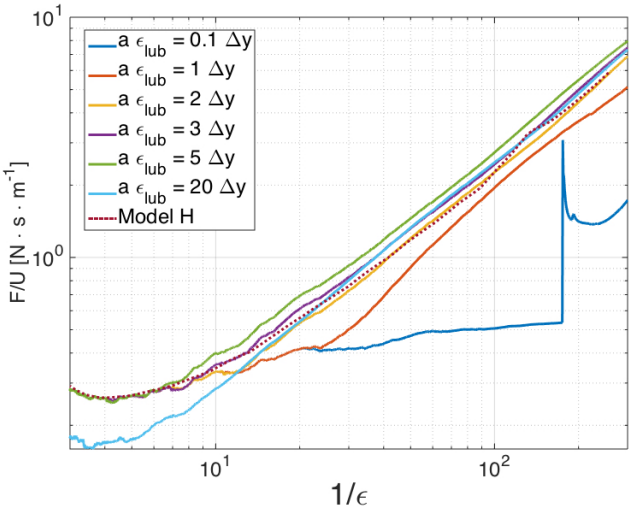

Figure 15: Total hydrodynamic force, according to the y-direction as a function of $1/\epsilon$ during the approach phase for the critical lubrication distances $a\epsilon_{\text{lub}}$ equal to $0.1\Delta y$, $1\Delta y$, $2\Delta y$, $20\Delta y$, $3\Delta y$, and $5\Delta y$ (respectively by increasing F/U at the highest $1/\epsilon$)
. Grid mesh resolution is $h = 1/40$ for all curves.

$1/\epsilon$.

Numerical simulations using $a\epsilon_{\text{lub}} \approx 2\Delta y$ are expected to give more realistic solutions since hydrodynamic forces better fit the model H solution. For smaller ϵ_{lub}, hydrodynamic forces are underestimated leading to unrealistic mechanical contact and rebound of the particle (particle rebounds are not allowed by viscous effects for $St < 10$). Simulations with high ϵ_{lub} underestimate the total hydrodynamic force far from the wall, which decreases the solution accuracy.

The configuration of ϵ_{lub} depends *a priori* of the spatial discretization of the Navier-Stokes equations, and needs to be adapted to the numerical method. This configuration can be easily done by running a sensitivity analysis from ϵ_{lub}, as shown in this section.

5.1.4 Analysis of the LLCM reliability during collision

To complete our model reliability assessment, several simulations had been performed at higher Stokes numbers and compared to experimental data from Joseph *et al.*[38].

The conservation of the energy by LLCM and the collision model have been checked by simulating the normal collision of a steel particle with a wall (see figure 16). When the particle is assumed elastic ($\xi_{\text{max,n}} = 1$) the energy is conserved during the collision. Otherwise, energy dissipation due to plastic effects from the collision model are observed.

Figure 17 represents the distribution of the normalized effective coefficient of normal restitution of a particle versus the impact Stokes number. In order to be comparable to the measurements, we use the same technique and definition of the coefficient of normal restitution ξ_{n}, detailed by Joseph *et al.*[38]. By definition $\xi_{\text{n}} = -U_{\text{R}}/U_{\text{T}}$ where U_{R} is the particle rebound velocity and U_{T} is the terminal velocity of the particle before the collision.

When the fluid does not influence the dynamics of the particle while colliding with an obstacle, the effective coefficient ξ_{n} is maximum and equal to the so called "dry coefficient of normal restitution" $\xi_{\text{max,n}}$. Experimental measurements reported in figure 17 show that "dry collision" occurs at Stokes numbers $St_d > 1000$ where lubrication forces become negligible compared to the

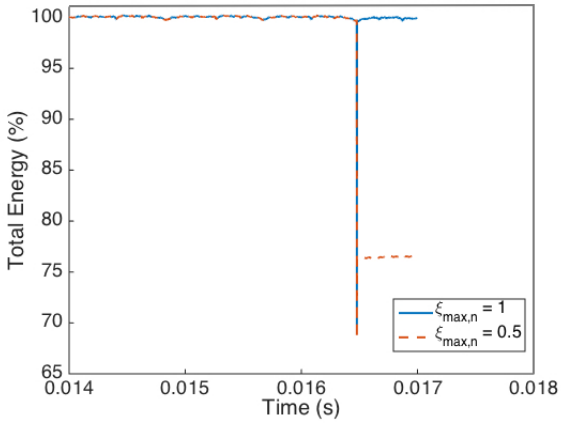

Figure 16: Evolution of the total energy (energy potential and kinetic) of the system during a elastic ($\xi_{\mathrm{max,n}} = 1$) or plastic ($\xi_{\mathrm{max,n}} = 0.5$) collision of a steel particle with a wall. In both cases the impact Stokes number is $St_d \approx 6900$.

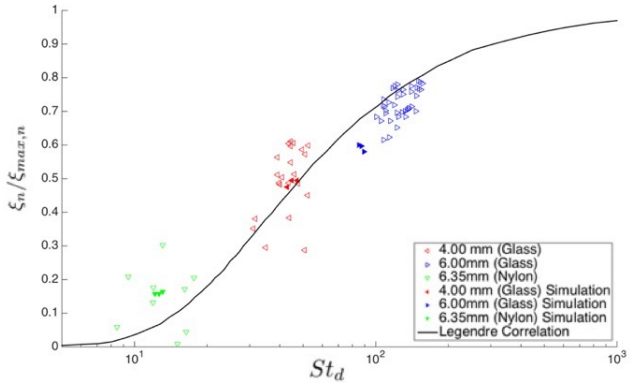

Figure 17: Distribution of normalized effective coefficient of normal restitution $\xi_{\mathrm{n}}/\xi_{\mathrm{max,n}}$ of a single particle impacting a wall in respect of the particle Stokes number at the impact. Filled markers represent results obtained using LLCM using the same experimental setup than Joseph *et al.*[38] (data represented by hallow markers). The black curve represents a correlation made on experimental data proposed by Legendre *et al.*[39]

particle inertia. At low Stokes numbers $St_d \lesssim 200$ lubrication forces are dominant. For $St_d \sim 10$ lubrication effects prevent solid collision with the wall and maintain the particle in "suspension" above the wall.

Results with the local lubrication model (figure 17) are comparable to measurements and have a strong correlation with the experiment at a low Stokes number.

5.2 Oblique Impact of a Particle on a Wall

In order to validate the tangential component of the lubrication force, the oblique impact of a particle on a wall is the last case to validate our model. The same experimental setup than Joseph and Hunt[40], for oblique particle-wall collisions in the air and aqueous solutions, has been

used.

A single particle is immersed in a domain $[19d, 5d, 3d]$ using a similar set-up than in section 5.1. The fluid is initially at rest and the particle is dropped without initial velocity as shown figure 18. In order to reproduce the experiment of Joseph and Hunt[40] the particle is linked to O by a virtual string of length $L = 10$ cm. The tension of the string is a virtual force $\mathbf{F}_i^{\mathrm{T}}$ collinear to $\mathbf{e_0} = \frac{\mathbf{X}_O - \mathbf{X}_i}{\|\mathbf{X}_O - \mathbf{X}_i\|}$ is added to the particle dynamic equation (30). The signed value of $\left(\mathbf{F}_i^{\mathrm{T}} \cdot \mathbf{e_0}\right)$ is found such that:

$$\mathbf{U}_i \cdot \mathbf{e_0} = 0, \; \forall \, \|\mathbf{X}_O - \mathbf{X}_i\| \geq L + a, . \tag{50}$$

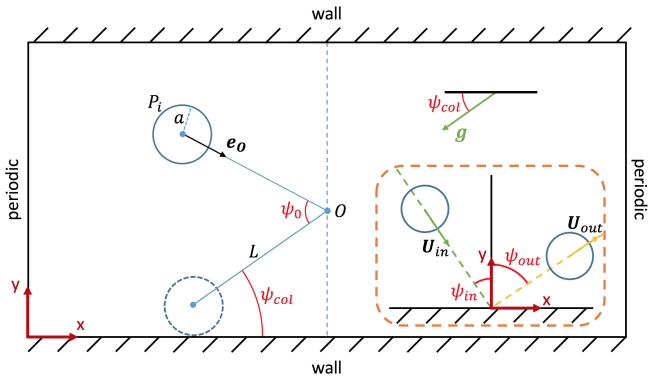

Figure 18: Sketch of the simulation domain and initial location of the particle. Inside the dashed box, particle characteristic velocities and angles are displayed before and after collision with the wall.

The pendulum is released from an angle $\psi_0 = 18°$ of its resting position ψ_{col} in contact with the wall (see figure 18). The gravity field $\mathbf{g}$ is oriented such that $\mathbf{g} = -g\left(\cos\left(\psi_{\mathrm{col}}\right)\mathbf{e_x} + \sin\left(\psi_{\mathrm{col}}\right)\mathbf{e_y}\right)$ and $g = 9.81 \text{ N} \cdot \text{kg}^{-1}$.

Physical properties of the particle are presented in table 3 and have been chosen similar to Joseph and Hunt[40] experiments.

		Glass	Steel	
Particle density	ρ_{p}	2540	7780	$\text{kg} \cdot \text{m}^{-3}$
Particle diameter	d	0.0127	0.0127	m
Normal restitution	$\xi_{\mathrm{max,n}}$	0.97	0.97	
Tangent restitution	$\xi_{\mathrm{max,t}}$	0.39	0.34	
Contact time	τ_{c}	$1 \cdot 10^{-7}$	$1 \cdot 10^{-7}$	s
Friction coefficient	μ_{c}	$0 \cdot 10$	0.11	
Friction coefficient (wet)	$\mu_{\mathrm{c,wet}}$	0.15	0.02	
Particle roughness	$a\epsilon_{\mathrm{col}}$	$2 \cdot 10^{-3}d$	$5 \cdot 10^{-4}d$	m

Table 3: Particle properties.

Numerical simulations using LLCM have shown that the parameter n_{lub}, introduced in the section 4, has a limited impact on the results when $n_{\mathrm{lub}} > 10$.

Figure 19 shows a comparison between the normalized incidence $\Psi_{\mathrm{in}} = \tan\left(\psi_{\mathrm{in}}\right)$ and rebound $\Psi_{\mathrm{out}} = \tan\left(\psi_{\mathrm{out}}\right)$ angles obtained from oblique collisions between steel and glass spheres in the

air or water. In practice, Ψ_{in} and Ψ_{out} have been assessed using the following equations:

$$\begin{aligned} \Psi_{in} &= -\frac{\mathbf{V}_{C,in} \cdot \mathbf{e_x}}{\mathbf{V}_{C,in} \cdot \mathbf{e_y}}, \\ \Psi_{out} &= \frac{\mathbf{V}_{C,out} \cdot \mathbf{e_x}}{\mathbf{V}_{C,out} \cdot \mathbf{e_y}}, \end{aligned} \tag{51}$$

with $\mathbf{V}_{\text{C,in}}$ and $\mathbf{V}_{\text{C,out}}$ the velocities of the particle at the contact point just before and just after collision respectively. ($\mathbf{V}_{\text{C}} = \mathbf{U}_i - a\,\mathbf{\Omega}_i \wedge \mathbf{e_y}$).

As highlighted by Joseph and Hunt[40], piezoviscous effects in wet collision modify the coefficient of friction. Therefore, the modified (wet) friction coefficient (see table 3) is considered when the particle is immersed in water.

Numerical simulations have been performed with $h = 1/40$ using $N_{\text{p}} = 3200$ particle mesh elements. Lubrication parameters have been chosen as $\epsilon_{\text{lub}} = 2$ and $n_{\text{lub}} = 100$.

Collisions of the particle immersed in the air are called dry collisions since the interactions between the solid particle and the surrounding fluid are negligible. Simulations of dry collisions have been performed (figure 19, top) to validate the collision model configurations and to assess the collision model accuracy with neglectable lubrication effects.

For wet collision (figure 19 bottom), hydrodynamic effects are no longer negligible. Therefore, the accuracy of the lubrication correction can be assessed. The numerical simulations are in good agreement with the experimental data for the entire range of incidence angles.

6 Conclusion and Outlook

A local lubrication correction model for particle laden flow of spherical solid particles has been presented and validated. Interactions between a particle and an obstacle (another particle or a wall) can be decomposed into three types: long range hydrodynamics, short range hydrodynamics also called lubrication effects, and mechanical solid-solid contacts.

Long range hydrodynamic interaction are fully resolved by the Volume Penalization method (VP). The incompressible Navier-Stokes equations have been discretized in time using a scalar projection method and in space with a fully second order penalty method.

Due to unresolved scales associated with the grid, short range hydrodynamic interactions are only partially captured by the numerical approach. We thus introduce a local lubrication model. This correction is based on asymptotic expansions of analytical solutions of particle-particle or particle-wall interactions, assuming that the flow within the gap between the particle and the obstacle is in the Stokes regime. Lubrication forces and torques are corrected in a neighborhood of the contact point of two interacting particles where lubrication is poorly captured, as long as the normalized gap width ϵ is smaller than a critical length ϵ_{lub} (a model parameter).

Finally, a linear soft-sphere collision model is used for solid-solid contacts. This model, widely used in the literature[29, 22], represents mechanical contacts as two spring-dashpot systems connected at the contact point. The model allows stretching the collision time, to avoid computational overhead in the calculation of the collision force, making the method particularly efficient.

Our local lubrication correction model have been validated on several benchmarks. First, we considered a single particle falling onto a wall at various approach velocities. The comparison with experimental results[35, 38] enables us to validate the dominant lubrication component resulting from the squeezing of the fluid in the gap. The lubrication force and the torque created by the shearing of the fluid in the gap have been validated on oblique particle-wall collisions in dry and

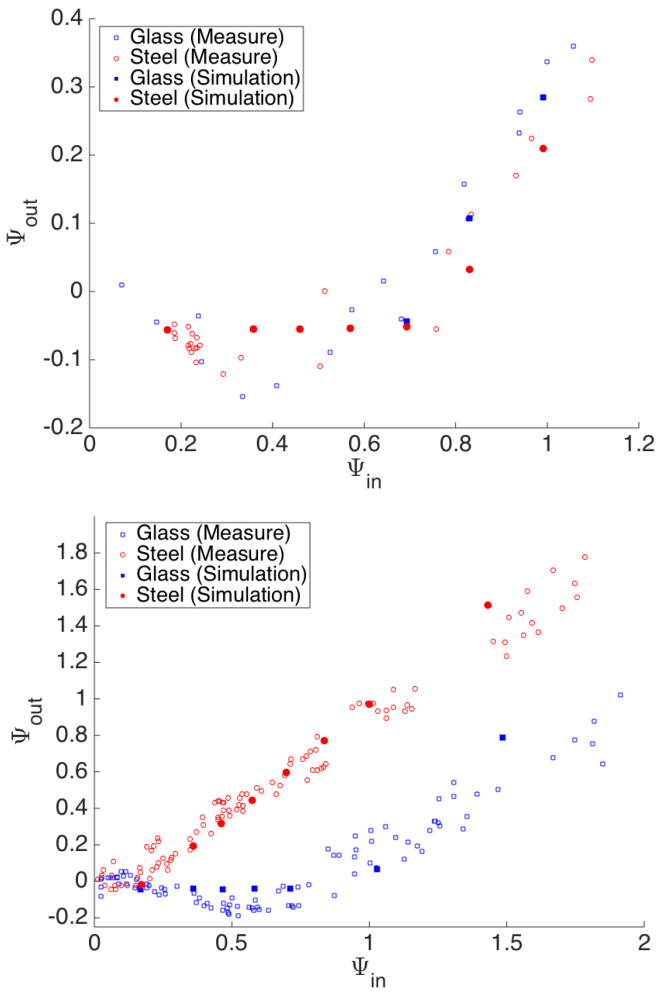

Figure 19: Comparison between the normalized incidence Ψ_{in} and rebound Ψ_{out} angles of steel (in red) and glass (in blue) particle in the air (on the top) or in aqueous solution (on the bottom) Results of simulations are represented by filled dots and are compared to Joseph and Hunt[40] experimental measurements (by circles).

wet systems proposed by Joseph and Hunt[40]. Since lubrication corrections are made locally, our lubrication model does not required tabulation and is compatible to non-spherical particles. The model will be tested for polydisperse flow of ellipsoidal particles in future works.

7 Acknowledgements

The simulations presented in this paper were carried out using the PLAFRIM experimental parallel testbed, being developed under the Inria PlaFRIM development action with support from LABRI and IMB and other entities: Conseil Régional dâAquitaine, FeDER, Université de Bordeaux and CNRS (see https://plafrim.bordeaux.inria.fr/).

References

[1] R. Sun and H. Xiao. CFD-DEM simulations of current-induced dune formation and morphological evolution. *Advances in Water Resources*, 92:228–239, 06/2016.

[2] J. Frohlich B. Vowinckel, T. Kempe and V. I. Nikora. *Numerical simulation of sediment transport in open channel flow.* Taylor & Francis Ltd, 2012.

[3] J. F. Morris R. Mari, R. Seto and M. M. Denn. Shear thickening, frictionless and frictional rheologies in non-brownian suspensions. *Journal of Rheology*, 58(6):1693–1724, 2014.

[4] A. Sierou and J. F. Brady. Accelerated stokesian dynamics simulations. *Journal of Fluid Mechanics*, 448:115–146, 12/2001.

[5] E. Climent and M. R. Maxey. Numerical simulations of random suspensions at finite Reynolds numbers. *International Journal of Multiphase Flow*, 29(4):579–601, 04/2003.

[6] M. R. Maxey and B. K. Patel. Localized force representations for particles sedimenting in stokes flow. *International Journal of Multiphase Flow*, 27(9):1603–1626, 09/2001.

[7] D. D. Joseph H. H. Hu and M. J. Crochet. Direct simulation of fluid particle motions. *Theoretical and Computational Fluid Dynamics*, 3(5):285–306, 09/1992.

[8] A. A. Johnson and T. E. Tezduyar. 3d simulation of fluid-particle interactions with the number of particles reaching 100. *Computer Methods in Applied Mechanics and Engineering*, 145(3-4):301–321, 05/1982.

[9] M. Martin S. V. Apte and N. A. Patankar. A numerical method for fully resolved simulation (frs) of rigid particle-flow interactions in complex flows. *Inst. Chem. Eng. Symp.*, 228(8):2712–2738, 05/2009.

[10] T. W. Pan R. Glowinski and J. Periaux. Distributed lagrange multiplier methods for incompressible viscous flow around moving rigid bodies. *Computer Methods in Applied Mechanics and Engineering*, 151(1-2):181–194, 01/1998.

[11] N. Sharma and N. A. Patankar. A fast computation technique for the direct numerical simulation of rigid particulate flows. *Journal of Computational Physics*, 205(2):439–457, 05/2005.

[12] J. A. Simeonov and J. Calantoni. Modeling mechanical contact and lubrication in direct numerical simulations of colliding particles. *International Journal of Multiphase Flow*, 46:38–53, 2014.

[13] A. Wachs. A DEM-DLM/FD method for direct numerical simulation of particulate flows: Sedimentation of polygonal isometric particles in a newtonian fluid with collisions. *Computers & Fluids*, 38(8):1608–1628, 09/2009.

[14] X. Shao Z. Yu and A. Wachs. A fictitious domain method for particulate flows with heat transfer. *Journal of Computational Physics*, 217(2):424–452, 09/2006.

[15] B. Merlet A. Lefebvre-Lepot and T. N. Nguyen. An accurate method to include lubrication forces in numerical simulations of dense stokesian suspensios. *Journal of Fluid Mechanics*, 769:369–386, 2015.

[16] A. J. C. Ladd and R. Verberg. Lattice-Boltzmann simulations of particle-fluid suspensions. *Journal of Statistical Physics*, 140(5):1191–1251, 09/2001.

[17] Z. G. Feng and E. E. Michaelides. Proteus: a direct forcing method in the simulations of particulate flow. *Journal of Computational Physics*, 202(1):20–51, 01/2005.

[18] M. Uhlmann. An immersed boundary method with direct forcing for the simulation of particulate flows. *Journal of Computational Physics*, 209(2):448–476, 11/2005.

[19] P. Angot, C.-H. Bruneau, and P. Fabrie. A penalization method to take into account obstacles in incompressible flows. *Numer. Math.*, 81(4):497–520, 1999.

[20] L. Lobry S. Gallier, E. Lemaire and F. Peters. A fictitious domain approach for the simulation of dense suspensions. *Journal of Computational Physics*, 256:367–387, 01/2014.

[21] M. D. A. Cooley and M. E. O'Neill. On the slow motion generated in a viscous fluid by the approach of a sphere to a plane wall or stationary sphere. *Mathematika*, 16(1):37–49, 1969.

[22] T. Bonometti E. Izard and L. Lacaze. Modelling the dynamics of a sphere approaching and bouncing on a wall in a viscous fluid. *Journal of Fluid Mechanics*, 747:422–446, 2014.

[23] J. Wells Y. Nguyen and H. Truong. A fictitious-domain simulation of solid-liquid flow with subgrid lubrication force correction; a sphere falling onto a plane surface. *Proceedings of Hydraulic Engineering*, 51:151–156, 2007.

[24] O. R. Walton. *Numerical simulation of inelastic, frictional particle-particle interactions.* Butterworth-Heinemann, 1993.

[25] S. Kim and S. Karrila. *Microhydrodynamics: Principles and Selected Applications.* Dover Publications Inc., 1991.

[26] D. J. Jeffrey. Low Reynolds number flow between converging spheres. *Mathematika*, 29(1):58–66, 05/1982.

[27] M. Stimson and G. B.Jeffery. The motion of two spheres in a viscous fluid. *The Royal Society*, 111(757), 05/1926.

[28] J. Happel and H. Brenner. *Low Reynolds Number Hydrodynamics.* M. Nijhoff, 1983.

[29] J. Westerweel P. Costa, B. J. Boersma and W. P. Breugem. Collision model for fully-resolved simulations of flows laden with finite-size particles. *Physical Review E*, 92(5), 10/2015.

[30] M. Bozkurttas F. M. Najjar A. Vargas R. Mittal, H. Dong and A. von Loebbecke. A versatile sharp interface immersed boundary method for incompressible flows with complex boundaries. *Journal of Computational Physics*, 227(10):4825–4852, 05/2008.

[31] A.J. Chorin. Numerical solution of the Navier-Stokes equations. *Math. Comp.*, 22:745–762, 1968.

[32] R. Temam. Sur l'approximation de la solution des équations de Navier-Stokes par la méthode des pas fractionnaires II. *Archiv. Rat. Mech. Anal.*, 32:377–385, 1969.

[33] Y. Saad and M. H. Schultz. GMRES: A generalized minimal residual algorithm for solving nonsymmetric linear systems. *Society for Industrial and Applied Mathematics*, 7(3):856–869, 07/1986.

[34] J. Hovnanian M. Bergmann and A. Iollo. An accurate cartesian method for incompressible flows with moving boundaries. *Communications in Computational Physics*, 15(5):1266–1290, 05/2014.

[35] T. Tanaka S. Harada and Y. Tsuji Tsuji. Fluid force acting on a particle falling toward a wall. *JSME International Journal Series B*, 44(4):520–525, 11/2001.

[36] M. J. Adams and V. Perchard. The cohesive forces between particles with interstitial liquid. *Inst. Chem. Eng. Symp.*, 91:147–156, 1985.

[37] S. L. Soo. *Fluid Dynamics of Multiphase Systems.* Blaisdell Publishing Company, 1967.

[38] M. L. Hunt G. G. Joseph, R. Zenit and A. M. Rosenwinkel. Particle-wall collisions in a viscous fluid. *Journal of Fluid Mechanics*, 433:329–346, 04/2001.

[39] C. Daniel D. Legendre and P. Guiraud. Experimental study of a drop bouncing on a wall in a liquid. *Physics of Fluids*, 17(9), 09/2005.

[40] G. G. Joseph and M. L. Hunt. Oblique particle-wall collisions in a liquid. *Journal of Fluid Mechanics*, 510:71–93, 2004.

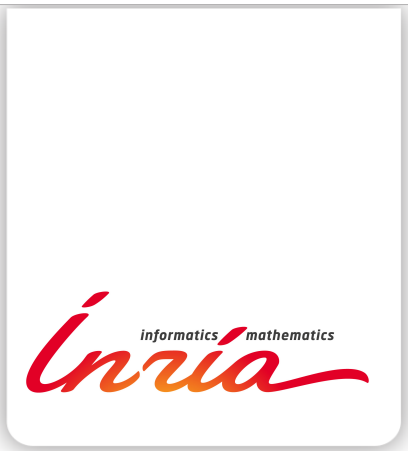

RESEARCH CENTRE
BORDEAUX – SUD-OUEST

200 avenue de la Vieille Tour
33405 Talence Cedex

Publisher
Inria
Domaine de Voluceau - Rocquencourt
BP 105 - 78153 Le Chesnay Cedex
inria.fr

ISSN 0249-6399